Effect of Impeller Design and Power Consumption on Crystal Size Distribution

Chinmay V. Rane
Dept. of Chemical Engineering, Inst. of Chemical Technology, Matunga, Mumbai, Maharashtra 400 019, India

Kalekudithi Ekambara
Dept. of Chemical Engineering, Inst. of Chemical Technology, Matunga, Mumbai, Maharashtra 400 019, India

Techno Force Solution (I) Pvt Ltd., D-33 MIDC, Nashik, Maharashtra 422 010, India

Jyeshtharaj B. Joshi
Dept. of Chemical Engineering, Inst. of Chemical Technology, Matunga, Mumbai, Maharashtra 400 019, India

Homi Bhabha National Inst., Anushaktinagar, Mumbai, Maharashtra 400 094, India

Doraiswami Ramkrishna
School of Chemical Engineering, Purdue University, West Lafayette, IN 47907

DOI 10.1002/aic.14541
Published online July 16, 2014 in Wiley Online Library (wileyonlinelibrary.com)

Crystallization processes in a 500 mL stirred tank crystallizer with computational fluid dynamics (CFD) and population balances toward estimating how crystal size distributions (CSDs) are influenced by flow inhomogeneities was explored. The flow pattern and CSD are presented here though extensive phase Doppler particle analyzer measurements and CFD predictions for three different impeller designs (disc turbine, pitched blade turbine, and Propeller) and each rotated at three different speeds (2.5, 5, and10 r/s). As crystallization processes in practice could involve break-up and aggregation of crystals, some selected break-up and aggregation kernels are incorporated. Extensive comparison of simulations with experimental data showed consistent trends in the proper quantitative range. An attempt has also been made to develop scaling laws: (a) mean particle size with average power consumption per unit mass and (b) particle-size distribution with the turbulent energy dissipation distribution. © 2014 American Institute of Chemical Engineers *AIChE J*, 60: 3596–3613, 2014
Keywords: crystallizers, computational fluid dynamics, crystal size distribution, phase Doppler particle analyzer, Flow field, stirred tank reactor

Introduction

Crystallization is one of the oldest unit operations known to mankind. Since the beginning of civilization, cooking salt has been produced by the evaporation of sea water. Even today solar evaporation is a still customary in regions with plentiful sunshine. The rise of the modern chemical industry and the increasing requirements for the quality and quantity of crystalline products were the triggers for the development of industrial crystallizers.[1] Crystallization processes are widely used in practically all the specialty and bulk chemical industries as a means of purification. However, the design procedures for crystallizers are still closer to an art than the desired state of science. Such a status is because of the complexity of fluid mechanics. As a consequence, the relationships between the crystal characteristics (mean crystal size, crystal size distribution, morphology, etc.) and fluid mechanics are yet to be understood. The supersaturation ratios and their special profiles affect the final crystal shape and size through their influence on the kinetics of nucleation and growth. They also affect crystal shape and morphology.[2] Given the underlying complexity of crystallization, it is still useful to study the different components individually toward subsequently coupling their effects. This article describes the role of some of the hydrodynamic parameters on crystal characteristics.

The main challenge in industrial crystallizers is to obtain the desired crystal-size distribution (CSD) and to predict the influence of vessel geometry, impeller design, operating conditions, and the effect of scale on the process behavior.[3,4] CSD control is important to ensure product quality and purity and the successful operation of the crystallizer. The final size distribution often affects downstream processing such as filtration, centrifugation, drying, milling, and formulation. In spite of its importance, the behavior of crystallizers and characterizing CSD for most processes is not well understood. Part of the complexity is that the size distribution varies in space and time in a crystallizer due to nonideal flow patterns and possible temperature distribution.

Correspondence concerning this article should be addressed to D. Ramkrishna at ramkrish@ecn.purdue.edu or J. B. Joshi at jbjoshi@gmail.com.

Process time scale, reactor opacity, and the inconvenience and intrusive nature of *in situ* experimental assessments are some of the formidable obstacles that prevent full understanding of the process dynamics within the stirred tank crystallizers.[3] An effective way of understanding crystallization behavior is through modeling. In the past, simple models such as mixed-suspension mixed-product removal models were developed.[1] These models predicted the CSD assuming that the crystallizer is well-mixed and the hydrodynamic effects were neglected. The assumption of ideality in the MSMPR model makes its application inappropriate to an industrial scale crystallizer as the particle concentration profiles (axial and radial) depend on the respective settling velocities of particles.[2] Further, it is practically impossible to achieve uniform supersaturation throughout the crystallizer. These two features result into limited applicability of these models. Nevertheless the models have been extensively used in designing crystallizers.[2] In fact, such empirical procedures are not completely reliable and call for overdesign. Obviously, they are not optimized for yield, CSD or morphology. In addition, in specialty industry the problems are acute because, in many cases, the existing hardware does not provide sufficient freedom. Further, the lack of understanding of the flow characteristics and crystallization kinetics make the process development and scale-up or scale-down a time consuming trial-and-error process.[2]

The kinetic parameters involved in crystallization, such as crystal growth rates, nucleation rates, breakage rates, and agglomeration rates depend upon many factors. Experimental crystallizers are used to determine the kinetic parameters to facilitate the design of industrial crystallization units. If the experimental data are poor for any reason, the design of the industrial unit does not ensure production of good quality product. The most significant factors affecting the kinetic parameters are the flow field, mixing behaviour, temperature fields, degree of supersaturation[3] and its special variation, and suspension density. Computational fluid dynamics (CFD) is a method to understand the hydrodynamics and was successfully used to investigate the roles of mixing, turbulence, and shear on the crystallizer performance.[5,6] CFD can provide an insight into the flow patterns generated by different impeller configurations[7] and hence on the concentration and temperature fields. These fields govern the crystallization rates and the CSD. However, it requires the CFD framework to be enhanced to include a detailed population balance (PB) to investigate the coupled effects of fluid mechanics and crystallization phenomena. The local crystal concentration may alter the local fluid properties and hence the hydrodynamics, which in turn influences the CSD. Population balance models (PBMs) that quantitatively monitor nucleation, growth, dissolution, aggregation and breakage make it possible to account for the coupling between the CSD and the hydrodynamics.

In this work, an attempt has been made to understand the flow pattern during the crystallization process (generated by different impeller designs at different speeds) and CSD through detailed experiments as well as CFD in a small-scale NaCl crystallizer. This study is a precursor to a treatment of industrial scale crystallizers in an upcoming publication.

Previous Work

The studies pertaining to crystallization in different types of crystallizers have been summarized in Table 1. Kramer et al.[8] have simulated evaporative forced circulation (FC) crystallizer of 200 L using a compartmental approach. They have assumed the flow pattern in the crystallizer to be unaffected by the presence of vapor. Further, they assumed isothermal conditions. They have concluded that the observed profiles were strongly affected by the choice of the kinetic parameters. In addition, they have brought out the importance of the step of validation by comprehensive comparison between the simulations and the experimental measurements of fields of supersaturation, crystal concentration and temperatures. Rousseaux et al.[9] have studied the effect of feed location, rotation speed, reactor geometry and reagent concentration on the CSD on precipatation of pseudoboehmite. The authors found good agreement between the experimental results and the CFD predictions while varying reactor geometry and reagent concentration. Zheng et al.[10] have studied the effect of feed locations, feed concentrations, impeller speed and residence time through CFD simulations on the precipitation of barium sulfate in a continuous stirred tank crystallizer. They found that, at high impeller speed, stronger turbulence at the feed location, lower feed concentration, and longer residence times were found to favor larger size of the particles during precipitation. The authors also investigated the effect of draft tube just above the impeller and varied the bottom clearance, diameter and height of the draft tube and found that the presence of the draft tube increases the mean crystal size. Logashenko et al.[11] investigated the crystallization of potassium nitrate in a continuous stirred crystallizer. The authors have shown the results of velocity, concentration of potassium nitrate, temperature, and crystal sizes at various time intervals in the form of contours. The authors have concluded that their simulations can be considered as a first step for solving many open issues.

Sha et al.[12] studied the factors affecting the size-dependent classification function by simulating the mixing process with different operating conditions in the crystallizer. They studied the spatial distribution of solids in the tank and classification function. It was concluded that the suspension density in the crystallizer affects the crystallization process. They have further shown that, in an imperfect suspension, continuous crystallization depends on both the mixing intensity and the product removal location. In addition, they have found that the different tank geometries have different efficiencies of classification. Zhu and Wei[13] have performed simulations of the batch crystallization of ammonium sulphate and observed that the velocity distribution did not change significantly when the particle phase was involved. Further, they found that the draft tube crystallizer with an axial impeller could provide a suitable flow field for a vacuum evaporation crystallization of ammonium sulphate. Wantha and Flood[14] have investigated the influence of the hydrodynamics in the DTB crystallizer, as characterized by the momentum source strength and fines removal flow, on the flow characteristics and the classification of crystals. They found that the overall magnitude of liquid velocity within the crystallizer can be strongly increased by increasing the axial momentum source but only slightly increased by increasing the fines removal flow rate. For the vapor phase, the overall magnitude of the velocity can be slightly increased by the axial momentum source and also slightly influenced by the fines removal flow rates. Plewik et al.[15] have simulated multiphase flow of monodispersed suspensions in various types of industrial crystallizers, namely, draft tube magma (DTM), double draft tube (DDT), and

Table 1. Previous Work

Author	Crystallizer Type	Geometry Details	Impeller Speeds and Other Details	Impeller Type	Grid Size	Model	Remarks
Kramer et al.[8]	FC crystallizer	200 L; $T = 0.3$ m; $H = 1.5$ m	Inlet low rate: 3 L/s	–	26 × 260	k-ε model FLUENT, SPEEDUP program	Compared one compartment and five compartment model was used. 2-D simulation as crystallizer is axis symmetric. No comparison with experimental results
Rousseaux et al.[9]	Stirred tank crystallizer	$T = 0.15$ m; $D = 0.12$ m; 2.5 L	1200, 1500 rpm	Common impeller	75 × 60 × 24	k-ε model; FLUENT 4.5	Studied effect of feed location, rotating speed and reagent concentration
Zheng et al.[10]	Continuous STR (precipitation of barium sulfate)	$T = 0.27$ m; $H = T$; $b = T/10$; $D = T/3$; $C = T/2$	200–500 rpm	Ruston turbine	36 × 72 × 90 (r,θ,z)	Standard k-ε model; In-house code	Compared crystal mean size by varying impeller speed, feed position, feed concentration and residence time. Also studied the effect of draft tube
Logashenko et al.[11]	Stirred tank crystallizer	0.2 × 0.2 m	Impeller speed simulated by source term	Common impeller	11,500 (2-D); 3,000 (3-D)	In-house code	Performed 2-D and 3-D simulationsNeglected crystal–crystal, crystal–wall collision
Sha et al.[12]	Stirred tank crystallizer with four-baffles with and without draft tube	1/4th tank $T = 0.15$ m; $H = T$	600, 1000, 1400 rpm; Particle sizes: 50, 100, 300, 500, 700, and 900 μm	Four-bladed propeller	34,400	k-ε turbulence model, SM CFX	Studied effect of impeller speed, product removal location and effect of crystallizer geometry
Zhu and Wei[13]	Stirred tank crystallizer with and w/o draft tube	200 mL and 300 L	200rpm for 200 mL; 200, and 600rpm for 300 L	Two blade and PBT	varied from 10,000 to 120,000	Standard k-ε model	Only flow field is given
Wantha and Flood[14]	Draft Tube Crystallizer (DTB)	$T = 1.05$ m; $H = 3.1$ m; 1.05 m^3	–	–	70000–82000	Standard k-ε model ANSYS CFX	Studied the characteristics of flow field, effect of momentum source strength and effect of fines removal flow rate on flow characteristics
Plewik et al.[15]	Fluidized Bed (FL), Double Draft Tube (DDT) and Draft Tube Magma (DTM)	$T = 0.68$ m; FL: $H = 0.83$ m; DDT: $H = 0.93$ m; DTM: $H = .83$ m	–	–	–	Standard k-ε model Fluent	Presented only axial velocity, volume fraction and fluid flow profiles though the three crystallizers. CFD data was analyzed for different geometry of tank and found to be within 10% deviation with LDA data

fluidized bed (FL) crystallizers. The CFD simulations were validated against experimental data using laser Doppler velocimetry measurements on a scaled down geometry which led to their conclusion that the multiphase computation method was a very useful tool for such analysis. They further found that hydraulic conditions in industrial crystallizers were far from ideal and increased mixing energy dissipation and caused increase in crystal destruction.

In the work of Derksen,[16] large-eddy simulations (LESs) of the turbulent flow driven by a Rushton turbine have been coupled to a Lagrangian description of spherical, solid particles immersed in the flow. The working fluid was water, whereas the solid particles had the properties of glass beads. The tank size was 10 L and relatively low solids volume fractions (up to 3.6%) were employed. Two sets of particles were considered with particle diameter of 0.30 and 0.47 mm, respectively. It has been investigated to what level of detail the particle motion needs to be modeled to meet Zwietering's just suspended criterion. It appeared to be essential to take particle–particle collisions into account, mainly because of their exclusion effect that prevents unrealistic buildup of particle concentrations closely above the bottom. The simulations give detailed insight in the behavior of the particles and in the way that the liquid flow is altered by the presence of the particles. The frequency and intensity of particle–particle collisions, and particle–impeller collisions, have been investigated. Joshi et al.[17–19] have critically analyzed the performance of a large number of turbulence models for prediction of flows generated by axial and radial flow turbines. They have presented detailed comparison of CFD predictions and the experimental measurements obtained at large number of locations in the stirred tank and over a wide range of tank sizes. Recently, Gimbun et al.[20] have extended the work of Derksen[16] and presented a detached eddy simulation (DES), a LES, and a $k-\varepsilon$ based Reynolds averaged Navier–Stokes (RANS) calculation on the single phase turbulent flow in a fully baffled stirred tank, agitated by a Rushton turbine. The DES used here is based on the Spalart–Allmaras turbulence model solved on a grid containing about a million control volumes. The standard $k-\varepsilon$ and LES were considered here for comparison purposes. Predictions of the impeller-angle-resolved and time-averaged turbulent flow have been evaluated and compared with data from laser doppler anemometry measurements. The effects of the turbulence model on the predictions of the mean velocity components and the turbulent kinetic energy are most pronounced in the (highly anisotropic) trailing vortex core region, with specifically DES performing well. The LES that was performed on the same grid as the DES appears to lack resolution in the boundary layers on the surface of the impeller. The findings suggest that DES provides a more accurate prediction of the features of the turbulent flows in a stirred tank compared with RANS-based models and at the same time alleviates resolution requirements of LES close to walls.

From the forgoing discussion, it is clear that most of the previous published literature is generally concerned with the flow pattern[12–19] in crystallizers rather than the process of crystallization itself. Hardly any information is available in the published literature on the prediction of the roles of impeller design and power consumption on CSD s. In view of this, it was thought desirable to undertake a systematic study pertaining to CFD simulation and experimental validation in three phases with increasing complexity: (1) effect of impeller design and power consumption (P/V) on particle-size distribution. In this phase, the supersaturation has been assumed uniform throughout the crystallizer. For this case, evaporative crystallizer has been selected, (2) in the second phase, the effect of supersaturation field will be investigated. However, relatively small concentration gradients (spacial) will be considered by selecting medium size crystallizer (say, 500 L). In this phase, the case of cooling crystallizer will be investigated. (3) In the third phase; steep gradients will be considered using large size crystallizer. In the second and third phases, the effects of impeller design and power consumption will also be investigated along with the supersaturation field.

This article is concerned with Phase 1 and an attempt has been made to combine nucleation and growth kinetics, CFD with PBM. The CSD, crystal volume fraction, axial, radial, and tangential liquid velocities, turbulent kinetic energy, and turbulent energy dissipation rates have been predicted using three different impellers (DT, PBT, and Propeller) and each rotated at three different impeller speeds (2.5, 5, and 10 r/s). The model predictions have been compared with the measurements using phase Doppler particle analyzer (PDPA).

Mathematical Modeling

Governing equations

The ensemble-averaged mass and momentum transport equations for each phase are given by the following equations. Nomenclature section provides a description of all the variables appearing in the differential equations.

Continuity equation of the kth phase

$$\frac{\partial}{\partial t}(\rho_k \in_k)+\nabla\cdot(\rho_k \in_k \mathbf{v}_k)=S_{\mathrm{m}} \tag{1}$$

where the kth phase refers either to the continuous liquid phase or the discrete solid phase.

Momentum Equation.

$$\frac{\partial}{\partial t}(\rho_k \in_k \mathbf{v}_k)+\nabla\cdot(\rho_k \in_k \mathbf{v}_k \mathbf{v}_k)=-\in_k \nabla p+\rho_k \in_k \mathbf{g}+\in_k \mu_k \nabla^2 \mathbf{v}_k+\mathbf{F}_{\mathrm{I}} \tag{2}$$

In Eq. 1, S_{m} is a source term that captures the aggregation and break-up processes. The right side of Eq. 2 describes the details of which have been given by Murthy et al.[19,21] Authors[19] has considered the following formulation of drag force

The drag force exerted by the dispersed phase on the continuous phase is calculated as

$$\mathbf{F}_{\mathrm{D}}=K_{\mathrm{sl}}(\mathbf{v}_c-\mathbf{v}_d) \tag{3}$$

where K_{sl} is the fluid–solid exchange coefficient and can be written in the following general form

$$K_{\mathrm{sl}}=\frac{\in_{\mathrm{s}}\rho_{\mathrm{s}} f}{\tau_{\mathrm{s}}} \tag{4}$$

where f is defined differently for the different exchange-coefficient models. The drag function due to Syamlal and O'Brien[22] gives a somewhat better prediction when compared with the other models and it is defined as

$$f=\frac{C_{\mathrm{D}} Re_{\mathrm{s}} \in_{\mathrm{l}}}{24 v_{\mathrm{r,s}}^2} \tag{5}$$

where the drag coefficient, derived by Dalla Valle,[23] is given by

$$C_D = \left(0.63 + \frac{4.8}{\sqrt{Re_s/v_{r,s}^2}}\right)^2 \quad (6)$$

This model is based on measurements of the terminal velocities of particles in fluidized or settling beds, with correlations that are a function of the volume fraction and relative Reynolds number[24]

$$Re_s = \frac{\rho_l d_s |\bar{v}_s - \bar{v}_l|}{\mu_l} \quad (7)$$

where the subscript l is for the lth fluid phase, s is for the sth solid phase, and d_s is the diameter of the sth solid phase particles/crystals.

Energy Equation.

$$\frac{\partial}{\partial t}(\rho E) + \nabla \cdot \mathbf{v}_k(\rho E + p) = \nabla \cdot \left[k_{eff}\nabla T - \sum_j h_j \mathbf{J}_j + \tau_{eff} \cdot \mathbf{v}_k\right] + S_h \quad (8)$$

The first three terms on the right-hand side of Eq. 8 represent energy transfer due to conduction, species diffusion and viscous dissipation, respectively. S_h includes the heat of chemical reaction, and any other volumetric heat sources.

Species Transport Equation. The conservation equation for the *i*th species

$$\frac{\partial}{\partial t}(\rho Y_i) + \nabla \cdot (\rho \mathbf{v}_k Y_i) = \nabla \cdot \left(\rho D_m + \frac{D_t}{Sc_t}\right)\nabla Y_i + R_i + S_i \quad (9)$$

where Y_i is the mass fraction of each species, Sc_t is the turbulent Schmidt number, D_m is molecular diffusion, D_t is the turbulent diffusivity, R_i is the net rate of production of species i by chemical reaction, and S_i is the rate of creation by addition from the dispersion phase plus any user-defined sources. The default Sc_t is 0.7. Joshi and Ranade[25] have discussed the current status of CFD simulations.

Turbulence modeling

For the continuous phase, the renormalized group (RNG) $k-\varepsilon$ model was applied. The governing equations for the RNG $k-\varepsilon$ model are

$$\frac{\partial}{\partial t}(\rho_l \in_l k) + \nabla \cdot \rho_l \in_l k \mathbf{v}_k = \nabla \cdot \in_l \left(\mu_l + \frac{\mu_t}{\sigma_k}\right)\nabla k + \rho_l \in_l (P - \varepsilon) \quad (10)$$

$$\frac{\partial}{\partial t}(\rho_l \in_l \varepsilon) + \nabla \cdot \rho_l \in_l \varepsilon \mathbf{v}_k = \nabla \cdot \in_l \left(\mu_l + \frac{\mu_t}{\sigma_\varepsilon}\right)\nabla \varepsilon + \rho_l \in_l \frac{\varepsilon}{k}(C_{1\varepsilon}P - C_2^*\varepsilon) \quad (11)$$

where $C_{2\varepsilon}^*$ is given by

$$C_{2\varepsilon}^* = C_{2\varepsilon} + \frac{C_\mu \eta^s (1 - \eta/\eta_o)}{1 + \beta\eta^s} \quad (12)$$

P is the rate of production of turbulence given by

$$P = \frac{\mu_t}{\rho}\left(\nabla \mathbf{v} + \nabla \mathbf{v}^T\right) : \nabla \mathbf{v} \quad (13)$$

$C_{2\varepsilon} = 1.68$, $C_{1\varepsilon} = 1.42$, $\sigma_k = 1.0$, and $\sigma_\varepsilon = 1.2$ are constants. Turbulent eddy viscosity, μ_t is computed from

$$\mu_t = \rho C_\mu \frac{k^2}{\varepsilon} \quad (14)$$

where $C_\mu = 0.0845$ and the difference between the RNG $k-\varepsilon$ model and the standard $k-\varepsilon$ model lies in the additional sink term in the ε equation.

PB modeling

The method of moments has been used to solve the PB as it allows modeling arbitrary kinetics involving nucleation, growth, aggregation and breakage. In addition, one can recover the CSD using available numerical techniques to invert the moments. The standard method of moments is an efficient alternative to the discrete PB approach. In this approach, the PB equation is transformed into a set of transport equations for moments of the distribution. This method has been used by several investigators[12–15,22–24,26,27] to investigate crystallization processes. Recently, this method has been extended and improved, leading to the quadrature method of moments (QMOM).[13]

The CSD is an essential criterion for assessing the properties and quality of the product. To predict the CSD, the PB equations need to be solved. In this work, we have used the QMOM method for the crystallization processes. The CSD can then be expressed in terms of these moments.[28] This approach is sufficient to provide information useful for engineering and design purposes.[29] The moments m_j of the CSD are computed according to the following moment transport equation, considering the first four moments[24]

$$\frac{\partial}{\partial t}(\rho m_j) + \nabla \cdot (\rho \mathbf{u} m_j - \Gamma_{eff}\nabla m_j) = \rho(\bar{B}_{ag,j} - \bar{D}_{ag,j} + \bar{B}_{br,j} - \bar{D}_{br,j}) + \rho J_0^j \dot{n}_0 + \rho j G m_{j-1},\ j = 0, 1, 2\&3 \quad (15)$$

where $\bar{B}_{br,j}$, $\bar{D}_{br,j}$, $\bar{B}_{ag,j}$, $\bar{D}_{ag,j}$ are, respectively, the birth and death due to break-up and aggregation of crystals. J is the nucleation rate and G is the growth rate. In the current simulations, aggregation, and break-up models have been neglected except for one case, and the results are discussed in the Results and Discussion section.

The moments m_j of the number density are calculated by the quadrature approximation

$$m_j = \sum_{i=1}^{N} w_i V_i^j, \quad j = 1, 2, \ldots, 2N-1 \quad (16)$$

The quadrature approximation of order N of the number density $n(V, \mathbf{r}, t)$ is defined by its N weights $w_i(\mathbf{r}, t)$ and N abscissas V_i, and can be calculated by its first $2N$ moments $m_0, m_1, m_2, \ldots, m_{2N-1}$. The number of scalars (moments) $2N$ for QMOM is significantly lower than the number of classes M for the discrete methods.[30]

Growth and nucleation

The crystal growth rate G, a parameter that measures how fast a crystal grows, is, for most systems, exponentially dependent on the supersaturation. However, the end result of the crystal size obtained in a crystallizer is not a matter only of the growth rate, but also of the nucleation rate, J (how many crystals take part in crystal growth), and the attrition rate (how easily crystals break, and how small are the broken fragments). The nucleation rate is also a function of the supersaturation, and is affected by supersaturation to a far greater degree than the growth rate. As a result of these very

complex relationships, the supersaturation at which a crystallizer will operate must be chosen with considerable care.

The crystal growth rate G, is calculated as functions of the supersaturation ratio S defined in Eq. 19, following[31]

$$G=k_g(S-1)^2 \tag{17}$$

where k_g is constants.

Nucleation occurs as either primary or secondary nucleation. Primary (homogeneous) nucleation occurs at the onset of crystallization, when the concentration of the solvent exceeds the metastable region. Secondary nucleation, which is caused by contacts between a crystal and another surface,[32,33] and occurs within the metastable region. Crystal-to-crystal and crystal-to-impeller contacts are the most common sources of secondary nucleation. Secondary nucleation is, therefore, affected by the mixing energy input to the crystallizer. Secondary nucleation is a complex phenomena and is not well understood. A general theory for the prediction of nucleation rates does not exist. The nucleation rate J, is calculated as a function of the degree of agitation (N), the suspension density ($\in$), and the supersaturation (S)[34]

$$J=k_n(S-1)^{2.77} \tag{18}$$

where $k_n=k_n^{'}\ N\in$, the parameters of this model are $k_n^{'}$, k, and j, which are the nucleation rate constant, the solid concentration exponent, and the flow parameter exponent, respectively.

The key parameter for determining these kinetics is the local supersaturation, S, which reflects the thermodynamic driving force for crystallization and is defined as

$$S=\text{Solute mole fraction}/\text{Solubility} \tag{19}$$

$$\text{Solubility}=0.000919T-0.199 \tag{20}$$

The moments are used to calculate the mass-average crystal mean size, d_{32}, as follows

$$d_{32}=\frac{\sum_{i=1}^{N} m_3 v_i}{\sum_{i=1}^{N} m_2 v_i} \tag{21}$$

where v_i is the volume of the ith cell.

Aggregation model

The aggregation kernel is modeled using the Luo and Svendsen[35] model. The general aggregation kernel is defined as the rate of particle volume formation as a result of binary collisions of particles with volumes V_i and V_j

$$a(V_i,V_j,\mathbf{r})=\omega_{ag}(V_i,V_j,\mathbf{r})P_{ag}(V_i,V_j) \tag{22}$$

where $\omega_{ag}(V_i,V_j,\mathbf{r})$ is the frequency of collision and $P_{ag}(V_i,V_j)$ is the probability that the collision results in aggregation. The frequency, based on projected area, is given by

$$\omega_{ag}(V_i,V_j,\mathbf{r})=\frac{\pi}{4}\left(d_i^2+d_j^2\right)n_i n_j \bar{u}_{ij}(\mathbf{r}) \tag{23}$$

where $d_i\equiv(6V_i/\pi)^{1/3}$ is the diameter of the particle of volume V_i assuming spherical shape, $\bar{u}_{ij}$ is the velocity of the ith particle relative to the jth particle which has volume V_j, and $\bar{n}_i$ and $\bar{n}_j$ are the number densities of particles of volumes V_i and V_j, respectively. Two physical mechanisms are behind the calculation of the relative velocity. The first is that of turbulent mixing. Assuming that the crystal sizes lie in the inertial range of turbulence, and the turbulence is isotropic, the mixing velocity $\bar{u}_{ij}^t$ of the two crystals can be expressed as

$$\bar{u}_{ij}^t=\left(\bar{u}_i^2+\bar{u}_j^2\right)^{1/2} \tag{24}$$

where the turbulent velocity in the inertial subrange of isotropic turbulence is $\bar{u}_i=1.43(\varepsilon d_i)^{1/3}$. The expression for the probability of aggregation is given by

$$P_{ag}(V_i,V_j)=\exp\left\{-C_1\frac{\left[0.75\left(1+x_{ij}^2\right)\left(1+x_{ij}^3\right)\right]^{1/2}}{(\rho_2/\rho_1+0.5)^{1/2}(1+x_{ij})^3}\mathrm{We}_{ij}^{1/2}\right\} \tag{25}$$

where C_1 is a constant of order unity, $x_{ij}\equiv d_i/d_j$, ρ_1 and ρ_2 are the densities of the primary and secondary phases, respectively, and the Weber number is defined as

$$We_{ij}\equiv\frac{\rho_1 d_i\left(\bar{u}_{ij}^t\right)^2}{\sigma} \tag{26}$$

The birth rate of group j due to aggregation of group i and group k crystal is

$$\bar{B}_{ag,j}=\frac{1}{2}\sum_{i=1}^{N} w_i \sum_{k=1}^{N} w_k (V_i+V_k)^j \tag{27}$$

The death rate of group j due to aggregation with other crystals is

$$\bar{D}_{ag,j}=\sum_{i=1}^{N} V_i^j w_i \sum_{k=1}^{N} w_k a(V_i,V_k,\mathbf{r}) \tag{28}$$

Break-up model

The Luo and Svendsen[35] breakage kernel encompasses both the breakage frequency and the PDF of crystals formed from breakage. The general breakage rate per unit volume is usually written as

$$\Omega_{br}(V,V',\mathbf{r})=g(V',\mathbf{r})\beta(V|V') \tag{29}$$

where the parent particle suffering breakage has volume- and the daughter particle has volume V. In the above expression, $g(V',\mathbf{r})$ is the spatially nonuniform breakage frequency, and $\beta(V|V')$ is the normalized daughter particle distribution function. For binary breakage, the $\beta(V|V')$ must be symmetrical with respect to $\frac{V}{V'}=0.5$. The general form is the integral over the size of eddies λ hitting the particle with diameter d (and volume V). The integral is taken over the dimensionless eddy size $\xi=\lambda/d$. The general form is

$$\Omega_{br}(V,V')=K\int_{\xi_{min}}^{1}\frac{(1+\xi)^2}{\xi^{11/3}}\exp\left(-b\xi^{-11/3}\right)d\xi \tag{30}$$

where the model parameters are assumed to be as below

$$K=0.923\varepsilon^{1/3}d^{-2/3}\varepsilon;\quad b=12\left[f^{2/3}+\left(1-f^{2/3}\right)-1\right]\sigma\rho^{-1}\varepsilon^{-2/3}d^{-5/3}$$

The birth rate of group j crystals due to break-up of larger crystals is

$$\bar{B}_{br,j}=\sum_{i=1}^{N} w_i\int_0^{\infty} V_j g(V_i,\mathbf{r})\beta(V|V_i)dV \tag{31}$$

The death rate of group j crystals due to break-up into smaller crystals is

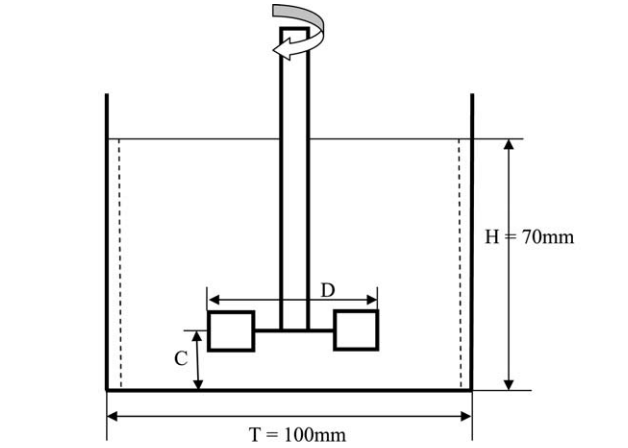

(A)

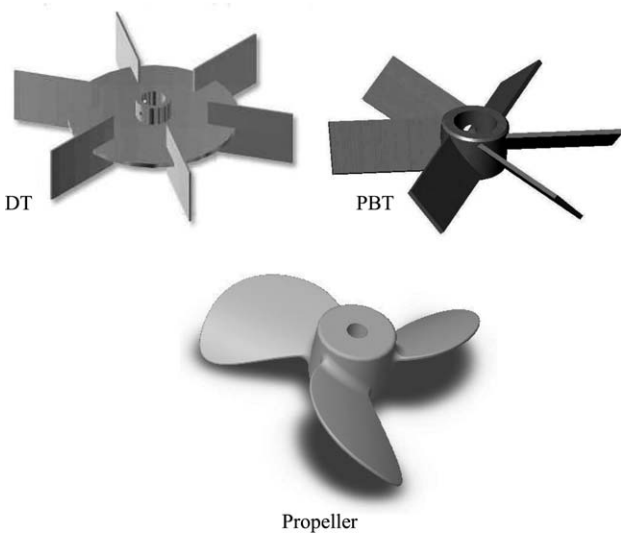

(B)

Figure 1. Geometry and impellers used for the study.

$$\bar{D}_{\mathrm{br},j} = \sum_{i=1}^{N} w_i V_i^j g(V_i, \mathbf{r}) \tag{32}$$

Geometrical details

Figure 1 shows the schematic structure diagram of the 500 mL stirred tank crystallizer with three impellers. The dimensions of the crystallizer are: diameters ($T = 0.1$ m) Height = 0.07 m. The clearance between the impeller and the vessel bottom was kept at 0.015 m and the impeller was centrally located. The height of liquid level (H) was equal to the tank height. Three types of impellers have been investigated by the CFD simulation and PDPA experiments, which include the disc turbine (DT), pitch blade turbine (PBT) and the propeller, the shape of the impellers as shown in Figure 1B. The geometrical details are given in Table 2.

Method of solution

The method of solution was the same as used by Murthy and Joshi.[21] Grid-independent study has been carried out only for the case of DT using two grid resolutions. The total number of cells in the three directions for the two cases, 115,000 ($\sim 35 \times 40 \times 80$, $z \times r \times \theta$) and 218,840 ($\sim 44 \times 50 \times 100$, $z \times r \times \theta$), respectively. It has been found that both the grids gave very similar profiles of turbulent kinetic energy and the values of power number were found to be practically the same. However, all the simulations have been performed for the grid resolution of 218,840 ($\sim 44 \times 50 \times 100$, $z \times r \times \theta$). The grid structure with all the three impellers is shown in Figure 2. In this work, simulations have been initially performed with the time step size of 0.00001 s. As the solution progressed the time step size has gradually been increased to 0.001 s to save computational time. The simulation was performed for a time span of 800 s. All the computations have parallely been performed on an IBM, 96 (eight nodes) processors cluster with a total 192 GB RAM, 2.63 GHz processor speed.

Boundary conditions

At the tank top, the atmospheric pressure was specified as boundary condition. No slip boundary conditions were used at all the impermeable walls. The mixture is initially at a temperature of 333 K and the walls are cooled at 253 K. The supersaturation ratio is defined as the ratio of concentration of NaCl in the solution to its solubility. The solubility curve of NaCl in water exhibits a linear dependency on temperature in the operating range. The growth (G) and nucleation (J) kinetics are based on power-law kernels are include using the user defined function in ANSYS FLUENT.[36]

Experimental Setup

Equipment

The schematic diagram of the experimental setup is shown in Figure 1A .The crystallizer (1) was of 100 mm impeller diameter (flat bottom) and 180 mm height and made up of glass. In all the experiments, initially, saturated sodium chloride solution (26 wt %) was taken in the crystallizer upto 70 mm height. The crystallizer was kept in a hot water bath

Table 2. Geometry and Numerical Details

Impeller Type	Tank Diameter, T (m)	Tank Height, H (m)	Impeller Speed (1/s)	Impeller Diameter, D (m)	Clearance from Bottom, C (m)	Grid Size
DT	0.1	0.07	2.5	0.05	0.015	218840
	0.1	0.07	5.0	0.05	0.015	218840
	0.1	0.07	10.0	0.05	0.015	218840
PBT	0.1	0.07	2.5	0.05	0.015	193363
	0.1	0.07	5.0	0.05	0.015	193363
	0.1	0.07	10.0	0.05	0.015	193363
Propeller	0.1	0.07	2.5	0.05	0.015	189533
	0.1	0.07	5.0	0.05	0.015	189533
	0.1	0.07	10.0	0.05	0.015	189533

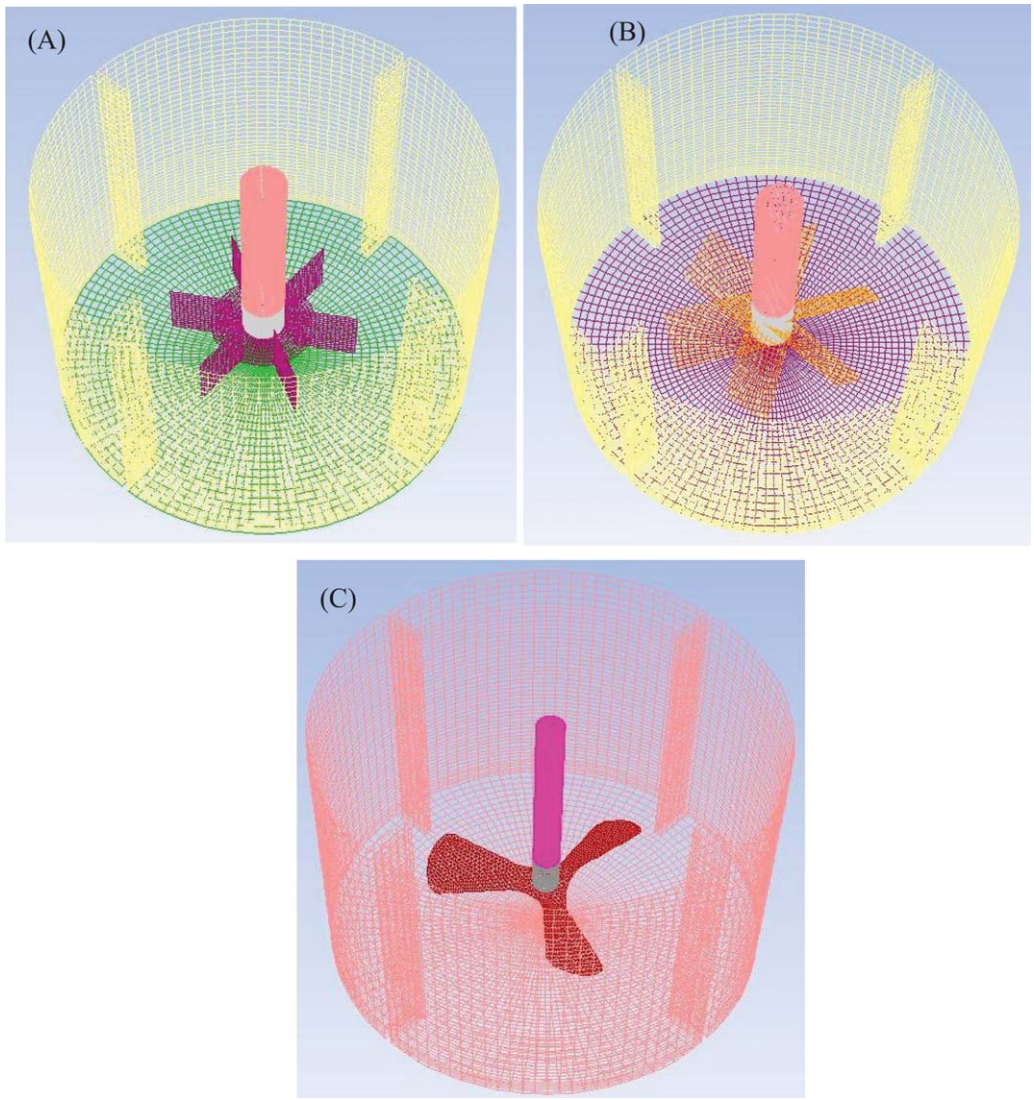

Figure 2. Grid structure for different impellers (A) DT, (B) PBT, and (C) Propeller.

[Color figure can be viewed in the online issue, which is available at wileyonlinelibrary.com.]

and slow evaporation was carried out at $58 \pm 2°C$ for a period of 6 h. Three impeller designs [DT, pitched blade turbine (PBT) and propeller were used. The impeller speeds were 2.5, 5, and 10 r/s for all the three impeller designs. The vessel was provided with four baffles of 10% width (3). All the impellers (centerline) were placed at 15 mm from the bottom. The impeller diameter was 50 mm in all the three designs. To reduce the curvature effect, the crystallizer was placed in a pentagonal tank (4). The dimensions and the location are given in Figure 1A. This tank also acted as a water bath. The elevation and plan of the crystallizer are shown in Figure 1B, where the measurement locations are highlighted.

Measurement

The velocity and crystal size measurements were performed by a laser Doppler anemometer (LDA), with a PDPA attachment, procured from Dantec Dynamics (Model No. 2017AR). The laser source was a 10 W Argon-ion laser. The laser probe and receiving optics were mounted on a lightweight traverse system. Three components of instantaneous velocity were measured at five axial locations (5, 15, 25, 35, and 50 mm from the bottom) and 19 radial locations (mid baffle plane) 2.5 mm gap. At the impeller center plane the number of radial locations were 9; first at 2.5 mm from the impeller tip and the other eight with 2.5 mm gap. The three instantaneous velocity components (axial, radial and tangential velocity) were normalized with the tip velocity. They were then plotted against normalized radial coordinates. The crystal size measurements were performed at the above mentioned positions. Refer Figure 3 for schematic diagram.

First of all, saturated salt solution with saturated concentration (the NaCl solubility is practically constant with respect to temperature) was filled in the crystallizer upto 70mm. The temperature in the crystallizer was maintained at $58 \pm 2°C$. The agitator was powered by 0.5 kW motor. Samples were taken over a period of 8 h. Each sample was subjected to centrifugation. The CSD of the solid phase was measured by sieving. It may be pointed out that the *in situ* measurements of PSD have also been undertaken using PDPA. The agreement between the sieving and the PDPA measurements was 10–26%.

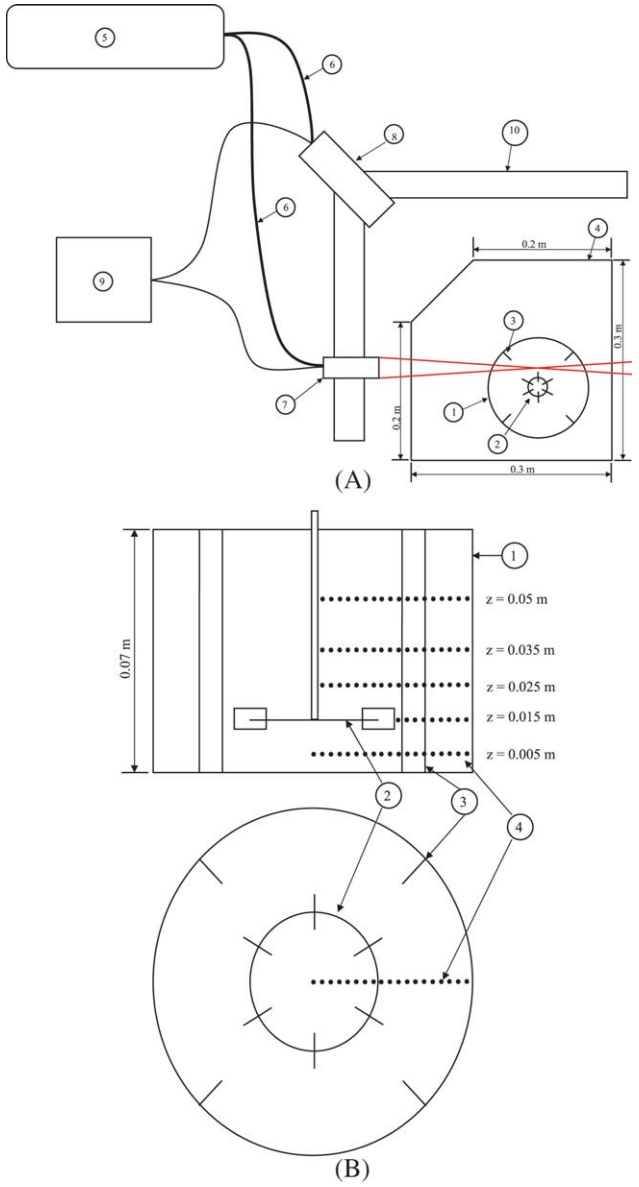

Figure 3. A (1) Crystallizer, (2) Impeller, (3) Baffles, (4) Pentagonal tank which also acts as water bath, (5) Laser Source and Optics, (6) Optical Fiber, (7) Laser Probe, (8) Optical receiver, (9) Computer, (10) Traverse system. B (1) Crystallizer, (2) Impeller, (3) Baffles, (4) Locations of measurement.

[Color figure can be viewed in the online issue, which is available at wileyonlinelibrary.com.]

Results and Discussion

The CFDsimulation results and the experimental measurements of the dimensionless mean axial velocity, mean radial velocity, mean tangential velocity, and mean turbulent kinetic energy have been plotted against the dimensionless radial distance. Further, the model predictions of the CSD have also been compared with the experimental data. Detailed discussion is given in the following sections.

Flow pattern

It was thought desirable to validate the CFD predictions of flow pattern before embarking on the prediction and measurements of CSD s. Although the measurements have been made at five axial and 20 radial locations, only some results have been shown for the sake of brevity.

Disc turbine

In the case of DT, the flow pattern generated by the impeller is a mixed radial-axial-tangential flow.[21,37] The quantitative and qualitative description of the flow generated by DT has been given by various authors.[38–41] Figures 4A–D, show the radial profile of mean axial, radial, tangential velocities and turbulent kinetic energy near the impeller region ($H = 0.025$ m). It is evident from the figures that the predictions of all the velocity profiles and k show good agreement (variation within 6–15%) with the experimental data. Similar good agreement was also found at other four axial locations with a standard deviation of 6–25%. It may be emphasized that the experimental measurements and CFD simulations have been performed in the presence of crystals. Further, simultaneously the CSD was also measured by PDPA.

Pitched blade turbine

For the PBT and for single phase flow various authors[41–44] have given comparison between the CFD predictions and the experimental measurements. In the presence of crystals, the normalized axial, radial, and tangential velocity components and normalized turbulent kinetic energy have been compared with the experimental data in Figures 5A–D. Very good agreement (variation within 4–18%) can be seen from these figures.

Propeller

For single phase flow, number of authors[45–48] have described the flows generated by axial flow impellers. In the presence of crystals, the flow generated by propeller has been plotted in Figures 6A–D in terms of radial profiles dimensionless axial, radial, and tangential velocity components and also turbulent kinetic energy. These figures show very good agreement (variation within 8–20%) with the CFD predictions. Again, we emphasize that the flow measurements in the present work have been performed in the presence of crystals and simultaneously the CSD has also been measured.

Overall flow pattern

In the previous section, an excellent agreement between the CFD predictions and PDPA measurements was shown at few locations for DT, PBT, and propeller in Figures 4–6, respectively. It may be pointed out that similar good quality agreements were found for all the impeller speeds covered in this work. The flow pattern with different impellers in the 500 mL stirred tank crystallizer is shown in Figure 7, which represents the velocity contours in the vertical center plane. It is observed that the DT produces strong radial discharge with intense swirling. In the case of axial flow impeller, PBT develops a strong downward flow with a tangential velocity component in the impeller region.[21] The uniformity of the liquid flow can clearly be depicted by the overall velocity contours. Further, it can be seen that the overall flow features are close to uniform at high impeller speed. Figure 8 shows the contours of the crystal mean volume fraction for the three impellers and impeller speed of 5 r/s. It can be observed that the

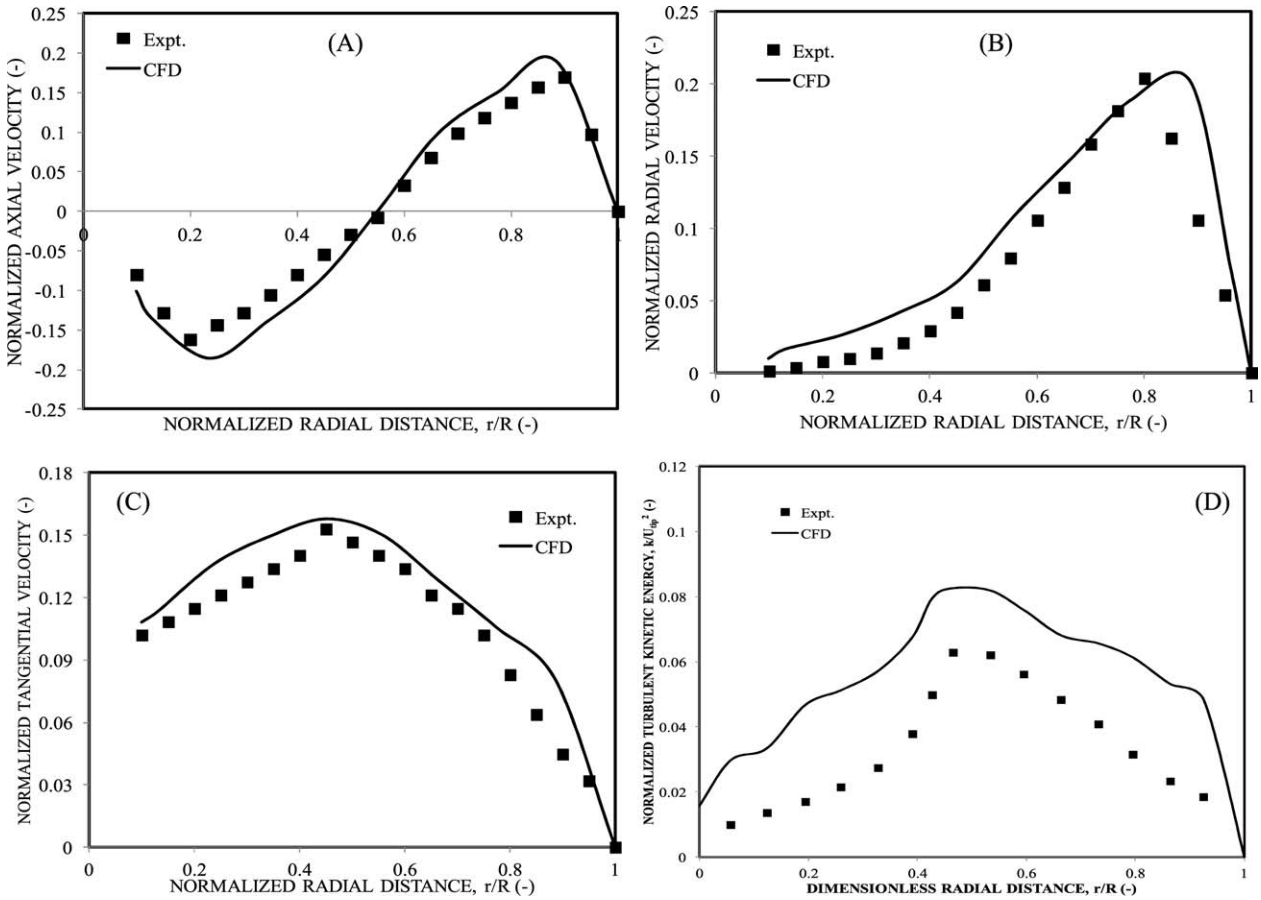

Figure 4. Flow pattern profiles for DT impeller at axial location, $H = 0.025$ m: (A) normalized axial velocity, (B) normalized radial velocity, (C) normalized tangential velocity, and (D) normalized turbulent kinetic energy.

volume fraction is more uniform with the propeller. Further, it may be noted that at low impeller speed (2.5 r/s), the crystal settling zone was found for all the three impellers.

Energy balance

Using CFD simulations, the values of energy dissipation rate (ε) were obtained for all the three impellers at all the impeller speeds. For instance, the radial profiles of ε for the propeller at five axial locations have been shown in Figures 9A–C. The total energy dissipation rate was calculated by volume integration of the predicted local turbulence energy dissipation rates (ε) as

$$\mathrm{P} = \frac{\int_0^{2\pi} d\theta \int_0^H dz \int_0^R r dr \varepsilon}{\int_0^{2\pi} d\theta \int_0^H dz \int_0^R r dr} \tag{33}$$

The values of actual energy total dissipation rates (power) for all the three impellers were obtained using the following equation

$$P = N_p \rho N^3 D^5 \tag{34}$$

where D is the impeller diameter and N is the impeller speed (r/s) of the stirrer. The power consumption was measured by using the procedure of Murthy and Joshi.[21] For this purpose, torque table was used. A precalibrated load indicator displays the load on the torque table. Ten readings were taken for each set and average was used for power measurement. Table 3 shows the comparison between the CFD predicted (Eq. 33) and the experimentally measured power consumption for all the three impellers and all the three impeller speeds. The predicted values show close agreement with the experimental values which implies good overall energy balance and also validity of the CFD simulations and the experimental measurements.

Crystal size distribution

The crystallization process consists of two major events, nucleation, and crystal growth.[3] Supersaturation is the driving force for crystallization; hence, the rate of nucleation and growth is driven by the existing supersaturation in the solution. Depending on the conditions, either nucleation or growth may be predominant over the other, and as a result, crystals with different sizes and shapes are obtained (control of crystal size and shape constitutes one of the main challenges in industrial manufacturing, such as for pharmaceuticals).

The appearance and size range of a crystalline product is extremely important in crystallization. If further processing of the crystals is desired, large crystals with uniform size are important for washing, filtering, drying, incineration, transportation, storage, and so forth. The importance lies in the fact that large crystals are easier to filter out of a solution than the small crystals. Also, larger crystals have a smaller surface area to volume ratio, leading to a higher purity. This higher purity is due to less retention of mother liquor which contains impurities, and a smaller loss of yield when the

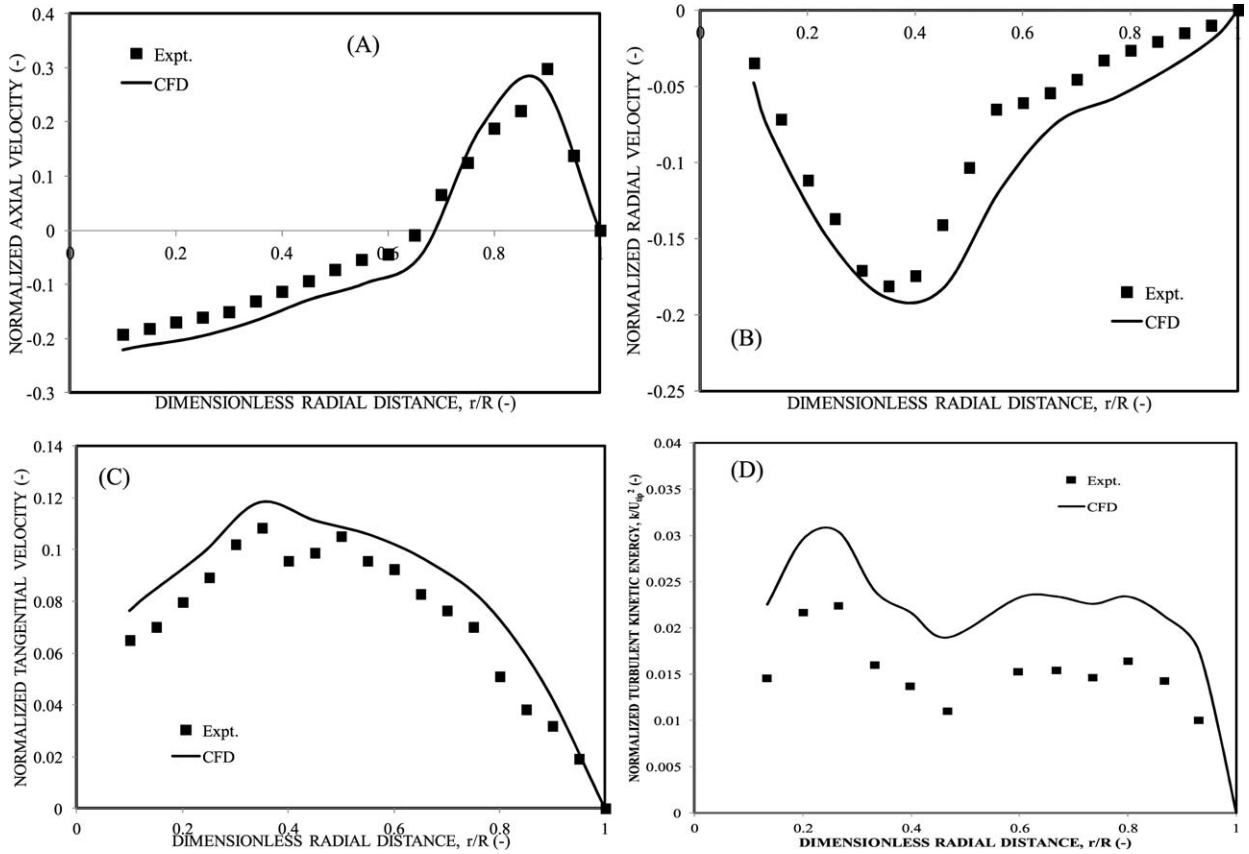

Figure 5. Flow pattern profiles for PBT impeller at axial location, $H = 0.025$ m: (A) normalized axial velocity, (B) normalized radial velocity, (C) normalized tangential velocity, and (D) normalized turbulent kinetic energy.

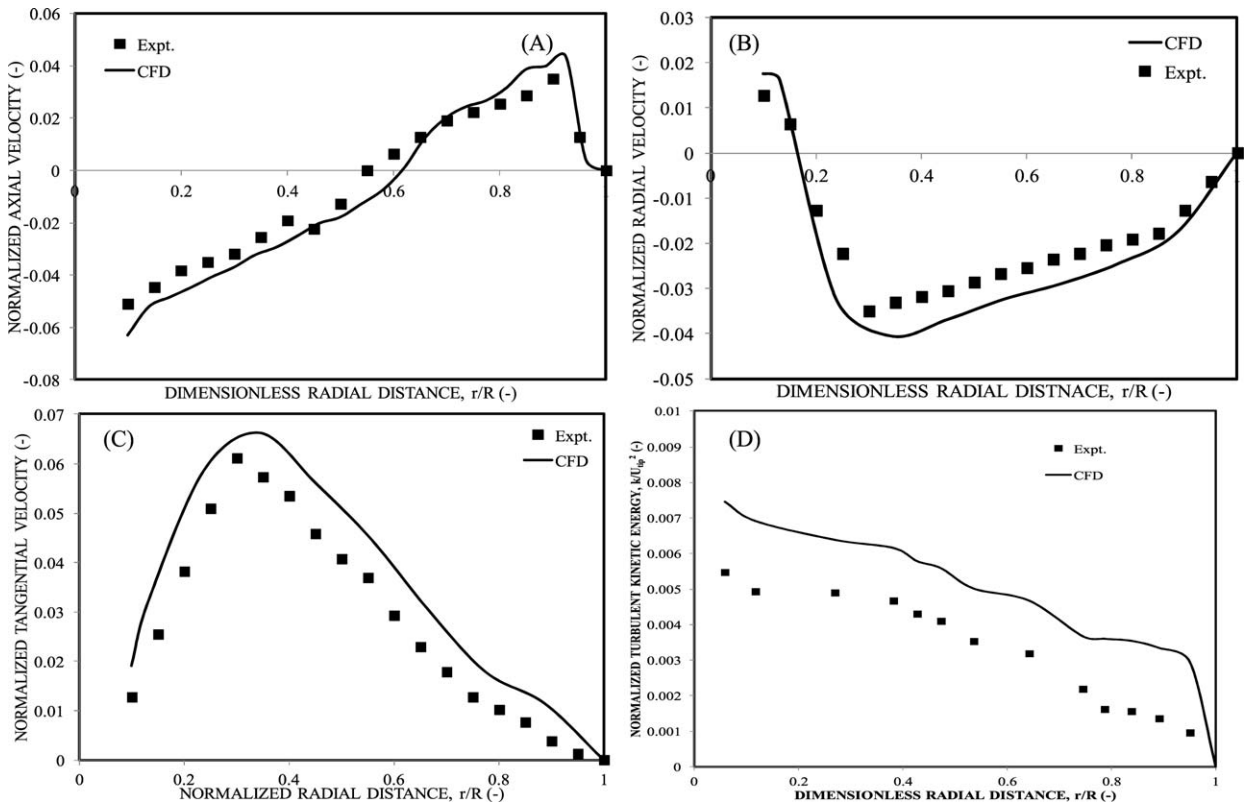

Figure 6. Flow pattern profiles for propeller at axial location, $H = 0.025$ m: (A) normalized axial velocity, (B) normalized radial velocity, (C) normalized tangential velocity, and (D) normalized turbulent kinetic energy.

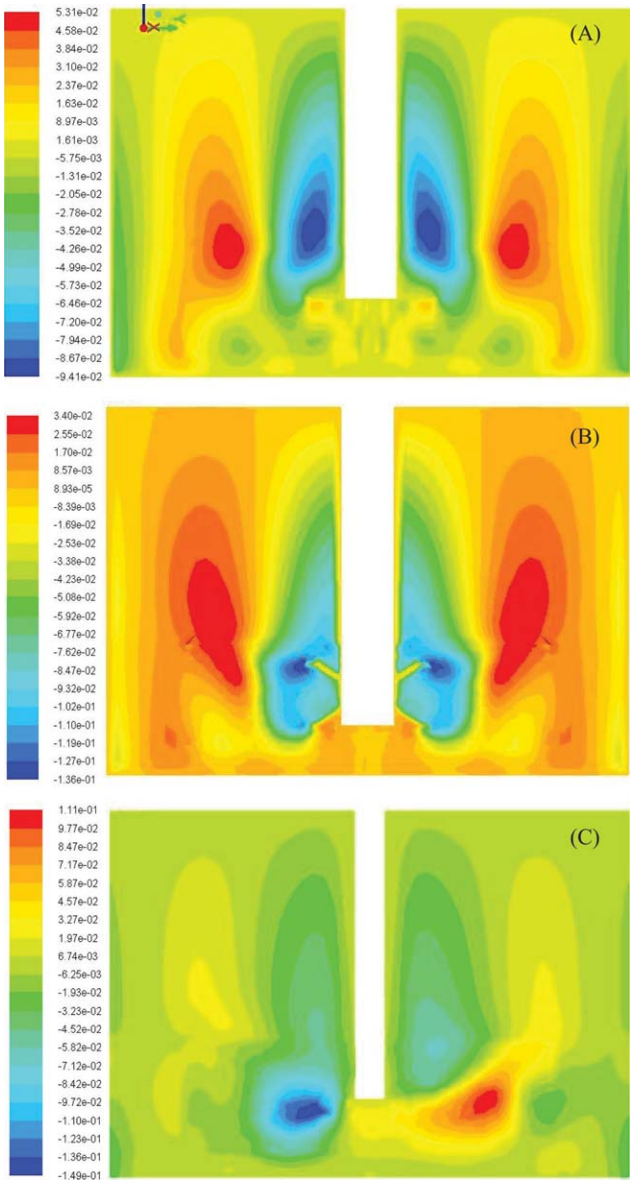

Figure 7. Contour plots of the axial velocity for (A) DT, (B) PBT, and (C) propeller.

[Color figure can be viewed in the online issue, which is available at wileyonlinelibrary.com.]

crystals are washed to remove the mother liquor. The CSD can be estimated as a function of operating conditions by using the PBM. In view of this, CFD-PBM coupled model has been used in the current simulation, including the nucleation, growth relations. Further, aggregation and break-up models were included along with nucleation and growth relations in PBM and the results will be discussed in separate section. Figures 10–12 demonstrate typical crystal concentration distributions in stirred tank crystallizer with three different impellers (DT, PBT, and propeller) and rotated at three different speeds. It can be observed that the predicted CSD shows reasonable agreement with the experimental data.

Effect of impeller speed on CSD

Impeller speed is a major parameter affecting the flow and crystallization process in a stirred tank crystallizer. Increasing the impeller speed tends to homogenize the concentration and the CSD in the tank by increasing both the pumping rate (i.e., convection) and turbulent diffusion. This in turn lowers the mean crystallize in the tank. To see the effect of impeller speed on the CSD, various simulations and experiments were carried out at three impeller speeds (2.5, 5, and 10 r/s) for DT, PBT, and propeller. The comparison of the predicted and the experimental results are shown in Figure 13. It can be seen that when the impeller speed is low (2.5 r/s), the CSD becomes wider. The reason appears to be partly due to the low supersaturation (because of low evaporation rate at low speed). At higher impeller speed (10 r/s), the suspension density for each size of the crystal tends to be uniform and the CSD of the product becomes narrow. An increase of the impeller speed enhances the rate of nucleation and as a result more nuclei get produced in the process environment. Therefore, high impeller speed causes production of crystals with small sizes as, in this case, the crystals experience more collisions and do not find the opportunity to have growth. Uniform flow also can lead to smaller spatial variations in

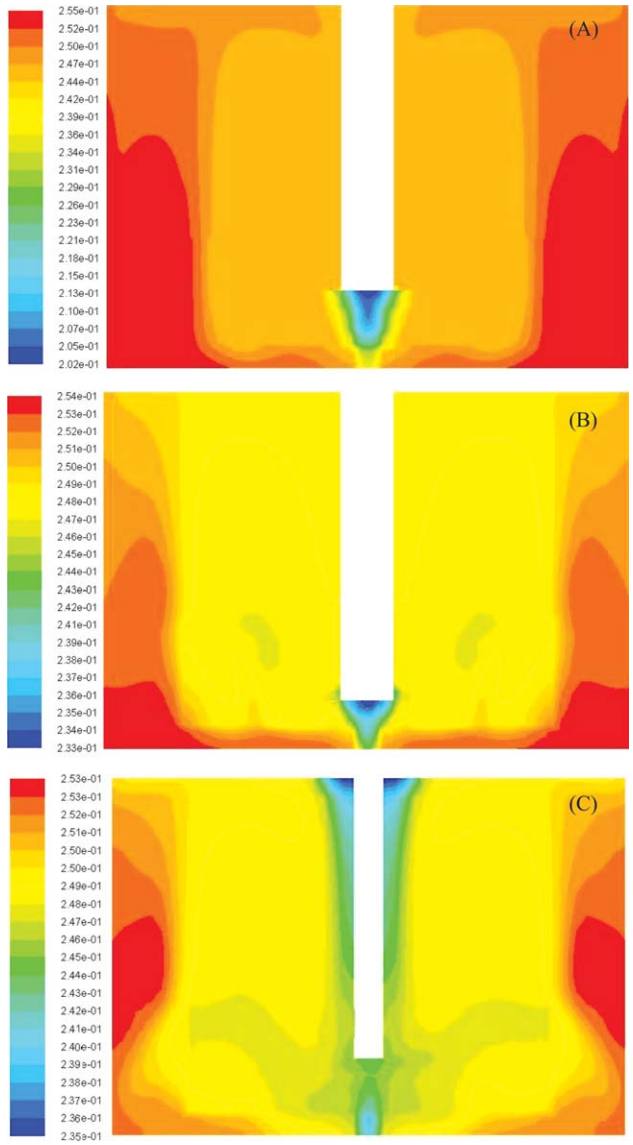

Figure 8. Contour plots of Crystal mean volume fraction for (A) DT, (B) PBT, and (C) propeller.

[Color figure can be viewed in the online issue, which is available at wileyonlinelibrary.com.]

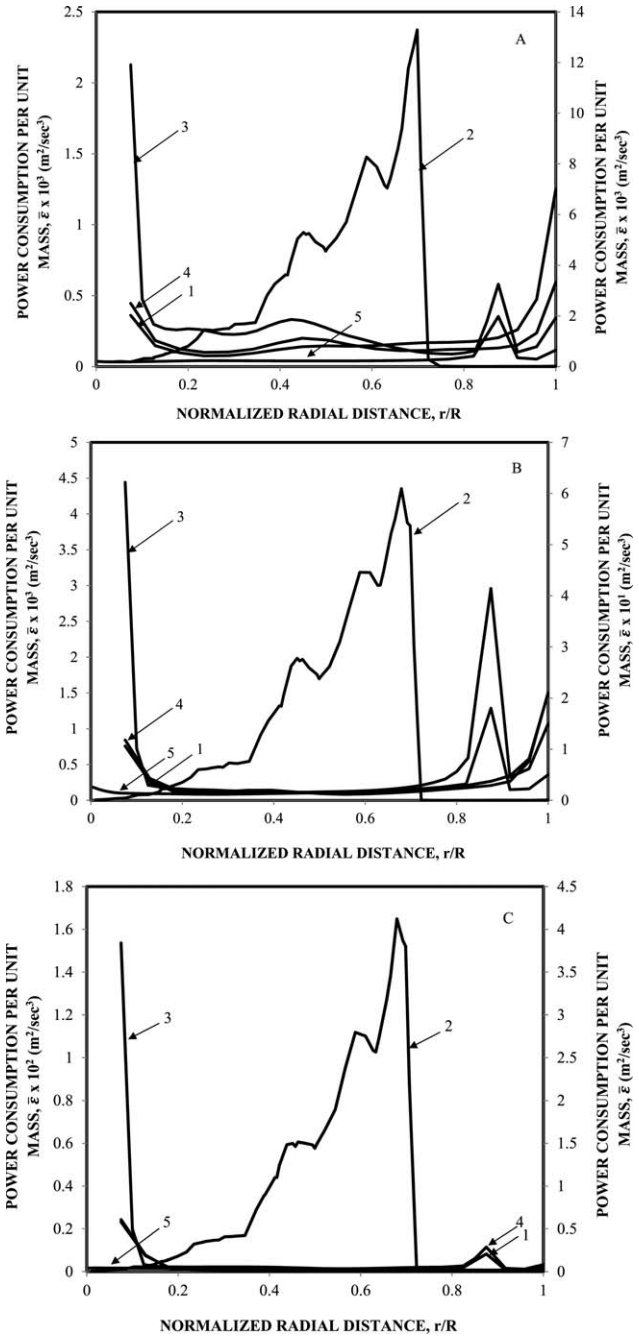

Figure 9. Power consumption profiles for propeller for (A) 2.5 rps, (B) 5 rps, and (C) 10 rps.

(1) $H = 0.005$ m, (2) $H = 0.015$ m, (3) $H = 0.025$ m, (4) $H = 0.035$ m, and (5) $H = 0.05$ m.

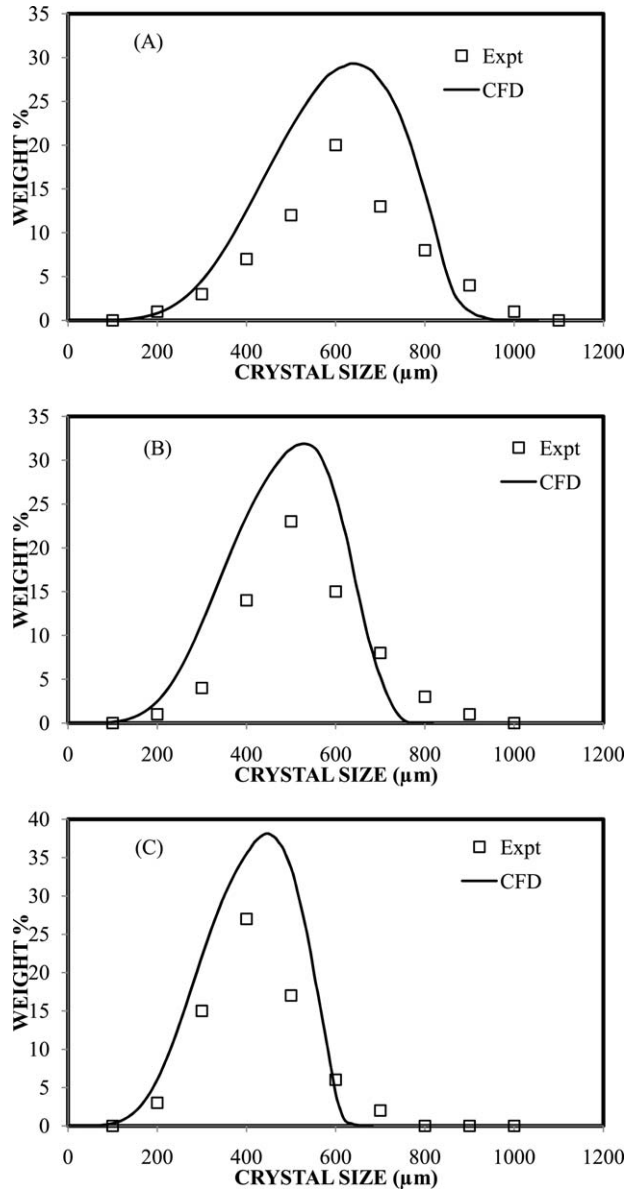

Figure 10. Comparison between the experimental and simulated profiles of CSD for DT at various impeller speeds (A) 2.5, (B) 5, and (C) 10 r/s.

the crystallization rate, in particular a more uniform crystal growth rate because the level of supersaturation in these areas will be constant.[14] It is also observed that the dominant size of the distribution decreases with an increasing impeller speed. Further, high specific power input improves mixing

Table 3. Crystal Size (Mean and Standard Deviation) and Energy Dissipation Rate (Mean and Standard Deviation)

Impeller Type	Speed (r/s)	Mean Crystal Size (microns)	Crystal Size Standard Deviation	Power Consumption from Expt. (watt)	Power Consumption from CFD (watt)	Power Consumption Standard Deviation
DT	2.5	532	304	0.0232	0.02583	0.116
	5.0	413	376	0.1805	0.20239	0.536
	10.0	344	463	1.4010	1.58488	7.049
PBT	2.5	544	263	0.0142	0.01564	0.036
	5.0	451	342	0.1115	0.12395	0.287
	10.0	378	386	0.6154	0.69037	2.328
Propeller	2.5	549	200	0.0033	0.00361	0.006
	5.0	467	250	0.0251	0.02770	0.033
	10.0	396	339	0.2101	0.23361	0.199

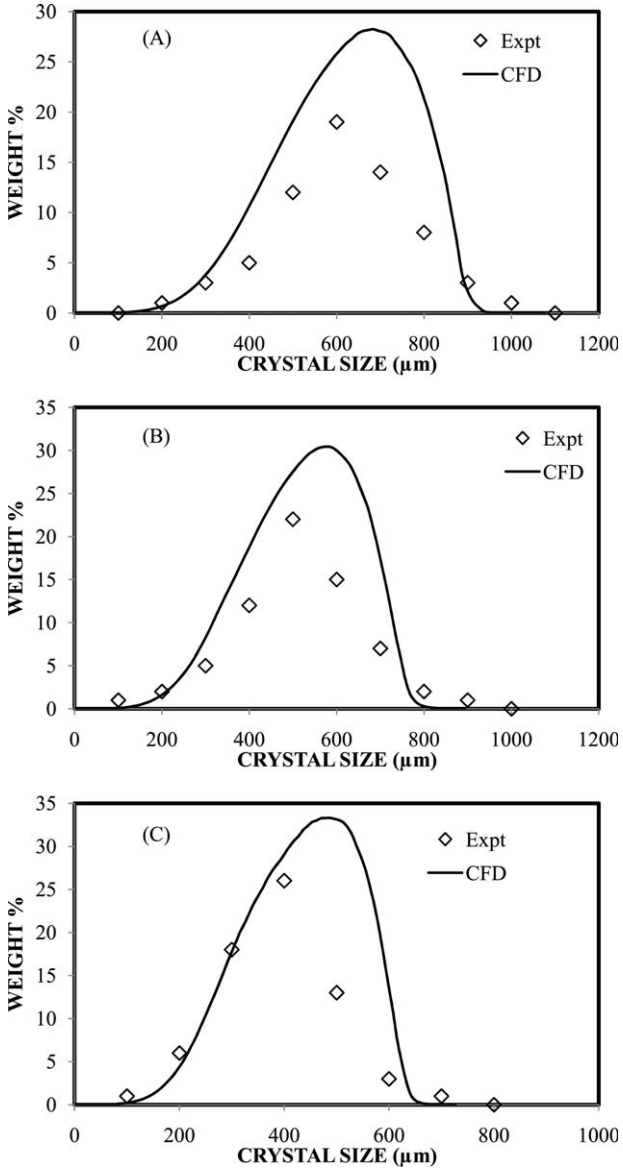

Figure 11. Comparison between the experimental and simulated profiles of CSD for PBT at various impeller speeds (A) 2.5, (B) 5, and (C) 10 r/s.

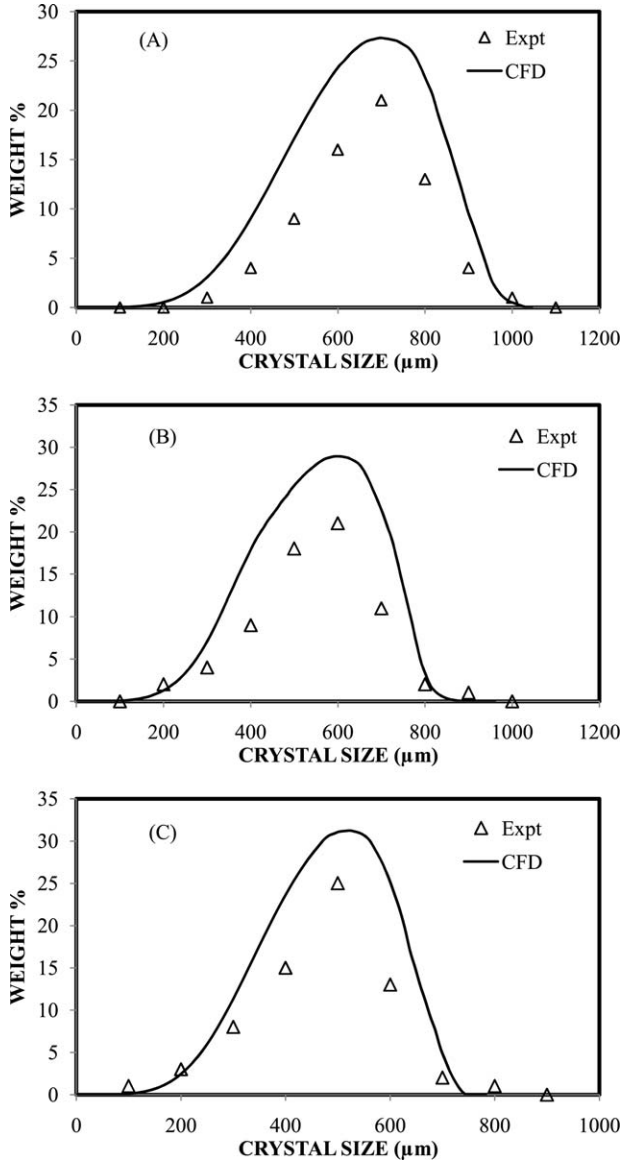

Figure 12. Comparison between the experimental and simulated profiles of CSD for Propeller at various impeller speeds (A) 2.5, (B) 5, and (C) 10 r/s.

and crystallizer homogeneity, which leads to the choice of the high impeller speed. Conversely, crystal damage and the control of secondary nucleation (which are strong functions of impeller shear rate) suggest the use of low impeller speeds. Therefore, the appropriate tradeoffs must be made to achieve sufficiently good mixing while minimizing crystal damage and managing secondary crystal nucleation.[34] The experimental results also show that the increasing impeller speed led to smaller mean crystal size of the sodium chloride, which are indeed consistent with the present simulation.

Effect of impeller design on CSD

Earlier it has been shown that DT, PBT, and Propeller generate different flow patterns, and hence, offer different efficiencies for the suspension operation and the mixing behavior. To understand the quantitative role of the impeller design on CSD, CFD simulations and the experiments have been carried out for the three impeller designs. The comparison of the experimental and the predicted CSD is shown in Figure 14. It can be observed that, PBT and propeller generate larger crystals than the DT. Table 3 shows the comparison of power consumption (energy dissipation rate) and the mean crystal size for different impeller designs and impeller speeds. The total energy dissipation rate depends on both the global mixing and the local mixing in the crystallizer. The energy dissipation rate can affect the growth rate of crystals by changing the mass-transfer rate and correspondingly, the mass-transfer rate of bulk solute to the crystal surface. It can be seen from Table 3 that the mean crystal size decreases with an increase in the energy dissipation rate/power consumption. Further, it can be observed that the propeller gives the larger crystals than the other two impellers (DT and PBT) at the same power consumption. The standard deviation of propeller is also the lowest as compared to the other impellers (DT and PBT).

Effect of aggregation and breakup models on CSD

To see the effect of aggregation and break-up models on CSD, various simulations were carried out with and without aggregation and break-up models in the PBM. Figure 15 shows the comparison of the experimental and the predicted CSD with and without aggregation and break-up models. The aggregation and break-up models used in this work increases crystal size because the effect of aggregation prevails over that of break-up. Further, it can be observed that the experimental data shows relatively better agreement with the CFD simulations with inclusion of aggregation and break-up models as compared with those predicted without the aggregation and break-up models.

It may be pointed out that, all the work (except Figure 15) does not include the use of any break-up or aggregation models. In particular, the important Figures 16 and 17 are also based on the predictions without any break-up or aggregation kernels. It may be emphasized that the CFD predictions agree with the experimental data with standard deviation of 19.5% and average deviation of 11.5%. When the break-up and aggregation models were included, the standard deviation and mean deviation diminished from 19.5 to 14.5% and from 16.18 to 11.5%, respectively.

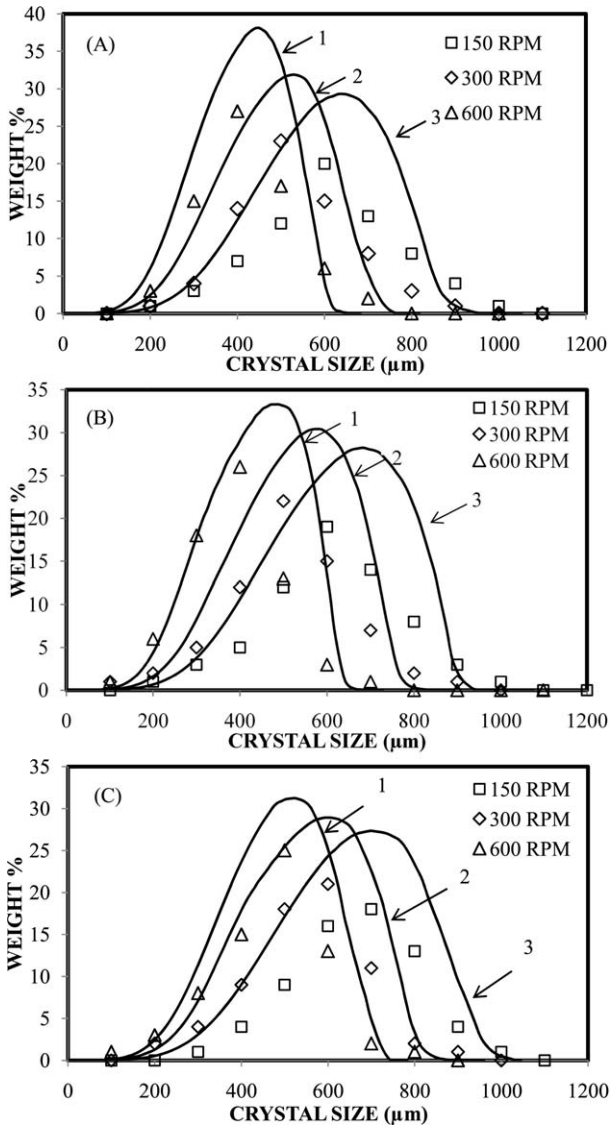

Figure 13. Effect of impeller speed on CSD for (A) DT, (B) PBT, and (C) propeller.

(1) 2.5 r/s, (2) 5 r/s, and (3) 10 r/s.

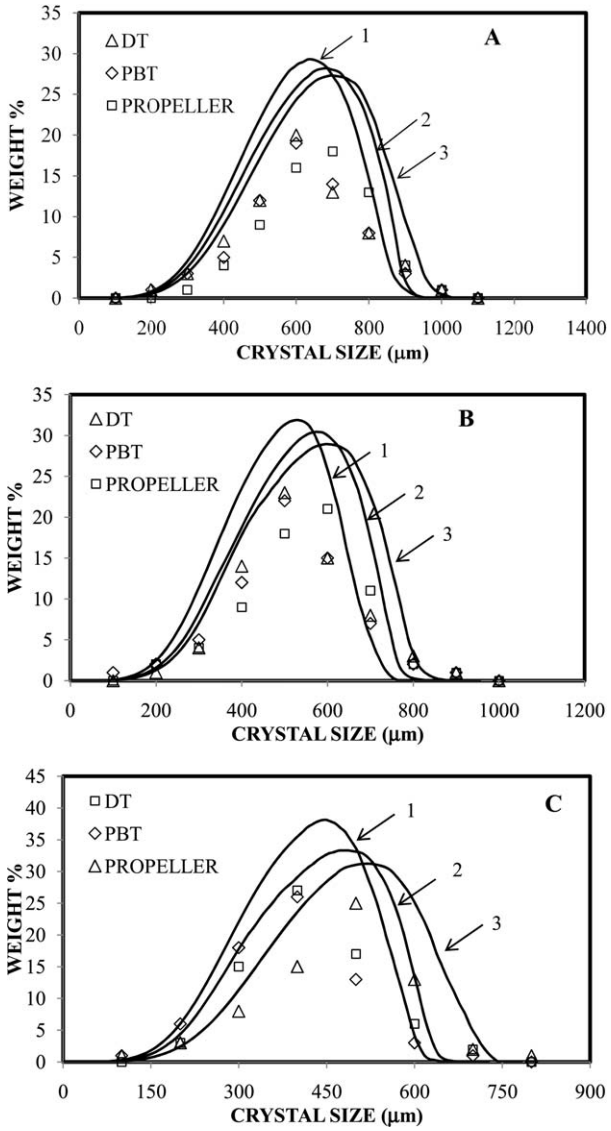

Figure 14. Effect of impeller design on CSD for (A) 2.5 r/s, (B) 5 r/s, and (C) 10 r/s.

(1) DT, (2) PBT, and (3) Propeller.

The investigation in this article must be regarded as an attempt to address complexities from various sources to decipher the behavior of industrial crystallizers. Comparison of simulations to observations must be made in the backdrop of uncertainties in measurement as well as in the phenomenological content of different model components. While quantitative predictions must await extensive future developments both in experiment and theory, current modeling in this area must be viewed in terms of its relevance to the behavior of complex equipment that can at best be semiquantitative. Thus, the adaptation of breakage and aggregation kernels for widely varying particle entities, while seemingly adventurous, could potentially serve to assess the relative importance of processes competing in a complex setting. Bhole et al.[49] have clearly brought out some of these issues.

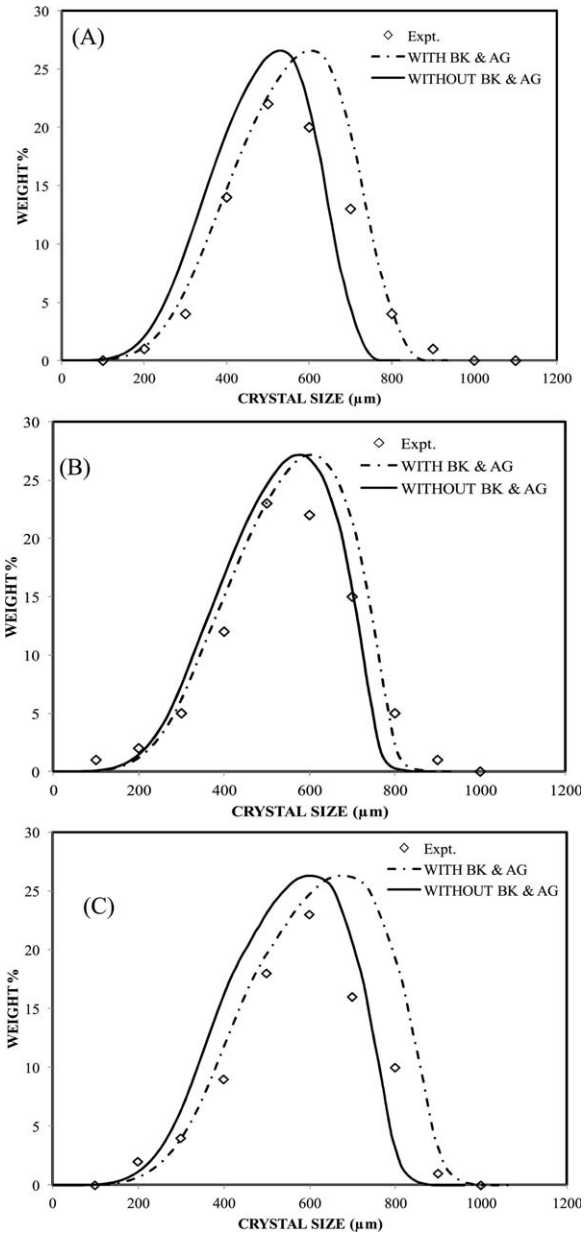

Figure 15. Effect of aggregation and break-up models on CSD at impeller speed of 5 r/s (A) DT, (B) PBT, and (C) propeller.

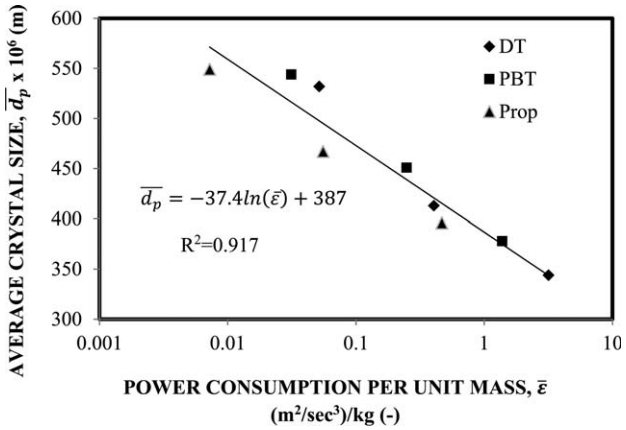

Figure 16. Effect of power consumption per unit mass on average CSD.

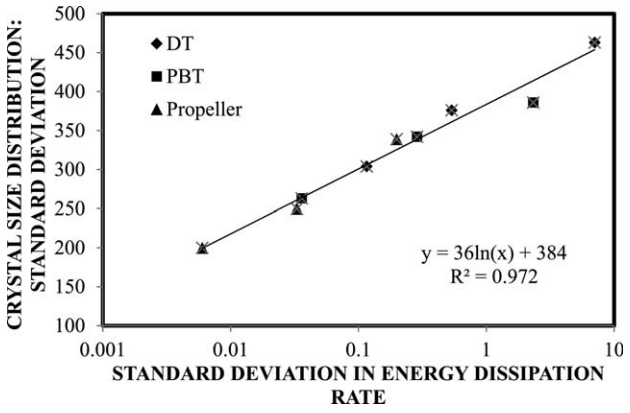

Figure 17. Dependence of particle-size distribution on the distribution of energy dissipation rate in the crystallizer, ◇ DT, ■ PBT, ▲ Propeller.

Effect of power consumption on mean crystal size and size distribution

The previous two sections describe the effects of impeller speed and the impeller design on CSD. It was thought desirable to see the effect of mean power consumption on mean particle size ($\bar{d}_p$). The results are given in Figure 16. The relation can be given by the following equation

$$\bar{d}_p = -37.4\ \ln(\bar{\varepsilon}) + 387 \tag{35}$$

it can be seen that, at a given value mean power consumption, the average particle size is independent of impeller design. However, as stated in the previous section, CSD becomes narrower as we use the impellers with lower power number, that is, CSD of DT > PBT > Propeller. This is because of the corresponding distribution of energy dissipation rate by the three impeller. The relationship between the standard deviation (y) in particle-size distribution and that in the energy dissipation rate (x) can be seen quantitatively in Figure 17. The relation can be represented by the following equation

$$y = 36 \ln(x) + 384 \tag{36}$$

The typical result of $\bar{d}_p$ to be independent of power consumption can be attributed to the method of evaporative crystallization. In this case, the supersaturation is uniformly generated throughout the crystallizer. Therefore, it is now proposed to see the effect of impeller design and power consumption on $\bar{d}_p$ and CSD for the case of cooling crystallization. For this case, there will be temperature field and hence the supersaturation field.

Conclusions

A RNG $k-\varepsilon$ model has been used to simulate the stirred tank crystallizer with three different impellers (DT, PBT, and Propeller) and all rotated at three impeller speeds (2.5, 5, and 10 r/s). In the CFD simulations, the nucleation and growth rates were used. A detailed comparison has been presented between the CFD predictions and the experimental data.

We also examined the sensitivity of PBMs with simple break-up and aggregation kernels. The predictions were found to improve with a standard deviation of 14.5% from 19.5% when the PB approach was not used.

The effects of impeller speed and impeller design on CSD were investigated in particular. The simulations show that the dominant size of the distribution decreases with increasing impeller speed. The experimental results for the mean crystal size of sodium chloride corroborate this observation. Further, it was observed that, thepropeller and PBT impellers generate larger crystals than the DT. In addition, it can be seen that the crystal size decreases with an increase in the energy dissipation rate (power consumption) and also it was found that the standard deviation of CSD by propeller is lower than the other impellers. We have noted two scaling laws to hold: (i) the mean crystal size depend on the mean power consumption ($\bar{\varepsilon}$) irrespective of the impeller design. (ii) The CSD was found to be directly related to the distribution of energy distribution rate (ε) in the crystallizer. Application of these methodologies results in understanding the complex processes behind crystallizations and gathering relevant data for scale-up in a short amount of time.

Tenneti et al.[50] have shown that the particle fluid interface hydrodynamics depends upon the particle velocity fluctuations. In turn, these as well as the critical impeller speed for solid suspension[51] depend on the dynamics of turbulent structures in the continuous phase. The research work on identification as well as quantification of turbulent structures is in progress.[52–54]

Notation

a, b, c_1, A_0, A_s = constants
B_{ag} = birth due to aggregation, defined in Eq. 29
B_{br} = birth rate due to break-up, defined in Eq. 33
c = instantaneous concentration of the tracer
C = impeller clearance from the tank bottom (m)
C_D = drag coefficient, define in Eq. 6
C_μ, $C_{\varepsilon 1}$, $C_{\varepsilon 2}$ = turbulence model parameters in the k-ε model
d = particle size (m)
d_{32} = mean crystal size (m)
d_s = particle diameter (m)
D = impeller diameter (m)
DDT = double draft tube
DT = disc turbine
DTM = draft tube magma
D_{ag} = death rate due to aggregation, defined in Eq. 30
D_{br} = death rate due to break-up, defined in Eq. 34
D_m = molecular diffusion (m^2/s)
D_t = the turbulent diffusivity (m^2/s)
$\bar{d}_p$ = mean particle size (μm)
f = defined in Eq. 5
F_D = drag force per unit area (N/m^3)
F_I = sum of the interfacial forces
FL = fluidized bed
g = acceleration due to gravity (m/s^2)
G = growth rate, defined in Eq. 19
H = liquid height (m)
J = nucleation rate, defined in Eq. 20
J_j = the diffusion flux of species j
k = turbulent kinetic energy (m^2/s^2)
k_{eff} = the effective conductivity
k_g = growth constant
k_n = nucleation constant
K_{sl} = fluid–solid exchange coefficient, defined in Eq. 4
k_t = the turbulent thermal conductivity
L = particle size (m)
m = momentum, defined in Eq. 17
n = number density
N = impeller rotation speed (1/s)
N_P = power number of the impeller
p = pressure (Pa)
P = power dissipation (W)
PBT = pitch blade impeller
r = radial coordinate (m)
R = radius of the vessel (m)
Re_s = relative Reynolds number, defined in Eq. 7
R_i = the net rate of production of species i by chemical reaction
S = supersaturation
Sc_t = the turbulent Schmidt number
S_i, S_h, S_m = source terms
t = time (s)
T = tank diameter (m)
T = temperature (K)
u' = mixing velocity (m/s)
U^* = friction velocity (m/s)
U_r = radial velocity (m/s)
v = velocity (m/s)
$v_{r,s}$ = terminal velocity of particles (m/s)
V = volume of the reactor (m^3)
w = weights
x = standard deviation in the energy dissipation rate
Y_i = the mass fraction of each species
y = standard deviation in particle-size distribution
z = axial coordinate (m)

Greek letters

$\in$ = volume fraction
ε = rate of turbulent energy dissipation (m^2/s^3)
$\bar{\varepsilon}$ = averagerate of turbulent energy dissipation (m^2/s^3)
μ = viscosity (Pa s)
μ_t = turbulent eddy viscosity (Pa s)
ρ = density (kg/m^3)
σ_k = Prandtl number for turbulent kinetic energy
σ_ε = Prandtl number for turbulent energy dissipation rate
Ω = break-up rate per unit volume, define in Eq. 31
ω = frequency collision, defined in Eq. 25

Subscripts and superscripts

ag = aggregation
br = break-up
c = continuous phase
d = dispersive phase
eff = effective
i, j, k = axis indexes of space coordinates
l = liquid
s = solids
t = turbulent

Literature Cited

1. Randolph AD, Larson MA. *Theory of Particulate Processes: Analysis and Techniques of Continuous Crystallization*, 2nd ed. New York: Academic Press, 1988.
2. Sha Z, Palosaari S. Mixing and crystallization in suspensions. *Chem Eng Sci*. 2000;55:1797–1806.
3. Mullin JW. *Crystallization*, 4th ed. London: Butterworth-Heinemann, 2001.
4. Xingfu S, Menghua Z, Jin W, Ping L, Jianguo Y. Optimization design for DTB industrial crystallizer of potassium chloride. *Ind Eng Chem Res*. 2010;49:10297–10302.
5. Liu X, Hatziavramidis D, Arastoopour H, Myerson AS. CFD simulations for analysis and scale-up of anti-solvent crystallization. *AIChE J*. 2006;52:3621–3625.
6. Vakili MH, Esfahany MN. CFD analysis of turbulence in a baffled stirred tank, a three-compartment model. *Chem Eng Sci*. 2009;64:351–362.
7. Pinelli D, Montante G, Magelli F. Dispersion coefficients and settling velocities of solids in slurry vessels stirred with different types of multiple impellers. *Chem Eng Sci*. 2004;59:3081–3089.
8. Kramer HJM, Dijkstra JW, Verheijen PJT, Van Rosmalen GM. Modeling of industrial crystallizers for control and design purposes. *Powder Technol*. 2000;108:185–191.
9. Rousseaux JM, Vial C, Muhr H, Plasari E. CFD simulation of precipitation in the sliding-surface mixing device. *Chem Eng Sci*. 2001;56:1677–1685.
10. Zheng W, Zaisha M, Chao Y, Xiangqian S. Computational fluid dynamics approach to the effect of mixing and draft tube on the precipitation of barium sulfate in a continuous stirred tank. *Chin J Chem Eng*. 2006;14:713–722.

11. Logashenko D, Fischer T, Motz S, Gillies ED, Wittum G. Simulation of crystal growth and attrition in a stirred tank. *Comput Vis Sci*. 2006;9:175–183.
12. Sha Z, Oinas P, Louhi-Kultanen M, Yang G, Palosaari S. Application of CFD simulation to suspension crystallization—factors affecting size-dependent classification. *Powder Technol*. 2001;121:20–25.
13. Zhu Z, Wei H. Flow field of stirrred tank used in the crystallization process of ammonium sulphate. *Sci Asia*. 2008;34:97–101.
14. Wantha W, Flood AE. Numerical simulation and analysis of flow in a DTB crystallizer. . *Chem Eng Commun*. 2008;195:1345–1370.
15. Plewik R, Synowiec P, Wojcik J, Kus A. Suspension flow in crystallizers with and without hydraulic classification. *Chem Eng Res Des*. 2010;88:1194–1199.
16. Derksen JJ. Numerical simulation of solids suspension in a stirred tank. *AIChE J*. 2003;49:2700–2714.
17. Joshi JB, Nere NK, Rane CV, Murthy BN, Mathpati CS, Patwardhan AW, Ranade VV. CFD Simulation of stirred tanks: comparison of turbulence models. part I: radial flow impellers. *Can J Chem Eng*. 2011;89:23–82.
18. Joshi JB, Nere NK, Rane CV, Murthy BN, Mathpati CS, Patwardhan AW, Ranade VV. CFD Simulation of stirred tanks: comparison of turbulence models. (part II: axial flow impellers, multiple impellers and multiphase dispersions). *Can J Chem Eng*. 2011;89:754–816.
19. Murthy BN, Ghadge RS, Joshi JB. CFD simulations of gas-liquid-solid stirred reactor: prediction of critical impeller speed for solid suspension. *Chem Eng Sci*. 2007;62:7184–7195.
20. Gimbun J, Rielly CD, Nagy ZK, Derksen JJ. Detached Eddy simulation on the turbulent flow in a stirred tank. *AIChE J*. 2012;58:3224–3241.
21. Murthy BN, Joshi JB. Assessment of standard k–e, RSM and LES turbulence models in a baffled stirred vessel agitated by various impeller designs. *Chem Eng Sci*. 2008;63:5468–5495.
22. Syamlal M, O'Brien TJ. Computer simulation of bubbles in a fluidized bed. *AIChE Symp Ser*. 1989:22–31.
23. DallaValle JM. *Micromeritics*. London: Pitman, 1948.
24. Richardson JR, Zaki WN. Sedimentation and fluidization: part I. *Trans Instit Chem Eng*. 1954;32:35–53.
25. Joshi JB, Ranade VV. Computational Fluid dynamics for designing chemical process equipment: expectations, current status and path forward. *Ind Eng Chem Res*. 2003;42:1115–1128.
26. Hulbert HM, Katz S. Some problem in particle technology: a statical mechanical formulation. *Chem Eng Sci*. 1964;19:555–574.
27. Bałdyga J, Orciuch W. Barium sulphate precipitation in a pipe—an experimental study and CFD modelling. *Chem Eng Sci*. 2001;56:2435–2444.
28. Öncül AA, Sundmacher K, Seidel-Morgenstern A, Thévenin D. Numerical and analytical investigation of barium sulphate crystallization. *Chem Eng Sci*. 2006;61:652–664.
29. Wei H, Zhou W, Garside J. Computational fluid dynamics modeling of the precipitation process in a semibatch crystallizer. *Ind Eng Chem Res*. 2001;40:5255–5261.
30. Rajniak P, Dhanasekharan K, Sinka C, MacPhail N, Chern R. Modeling and measurement of granule attrition during pneumatic conveying in a laboratory scale system. *Powder Technol*. 2008;185:202–210.
31. Jaworski Z, Nienow AW. CFD modelling of continuous precipitation of barium sulphate in a stirred tank. *Chem Eng J*. 2003;91:167–174.
32. Evans TW, Sarofim AF, Margolis G. Mechanisms of secondary nucleation in agitated crystallizers. *AIChE J*. 1974;20:950–958.
33. Evans TW, Sarofim AF, Margolis G. Models of secondary nucleation attributable to crystal-crystallizer collisions. *AIChE J*. 1974;20:959–966.
34. Myerson AS. *Handbook of Industrial Crystallization*, 2nd ed. London: Butterworth-Heinemann, 2002.
35. Luo H, Svendsen F. Theoretical model for drop and bubble breakup in turbulent dispersions. *AIChE J*. 1996;42:1225–1233.
36. Dhanasekharan K, Tsai K, Ring T. Using computational modeling to control and optimize the crystallization process. 2005. Available at: http://www.ansys.com//staticassets/ANSYS/staticassets/resourcelibrary/whitepaper/crystallization-wp107.pdf. Accessed October 1, 2012.
37. Alcamoa R, Micalea G, Grisafia F, Brucatoa A, Ciofalo M. Large-eddy simulation of turbulent flow in an unbaffled stirred tank driven by a Rushton turbine. *Chem Eng Sci*. 2005;60:2303–2316.
38. Khopkar AR, Rammohan AR, Ranade VV, Dudukovic MP. Gas–liquid flow generated by a Rushton turbine in stirred vessel: CARPT/CT measurements and CFD simulations. *Chem Eng Sci*. 2005;60:2215–2229.
39. Ranade VV, Joshi JB. Flow generated by a disc turbine I: experimental. *Chem Eng Res Des*. 1990;68:19–33.
40. Ranade VV, Joshi JB. Flow generated by a disc turbine II: mathematical model. *Chem Eng Res Des*. 1990;68:34–50.
41. Bakker A, Oshinowo LM. Modelling of turbulence in stirred vessels using large Eddy simulation. *Chem Eng Res Des*. 2004;82:1169–1178.
42. Ranade VV, Joshi JB. Flow Generated by pitched bladed turbine part I: experimental. *Chem Eng Commun*. 1989;81:197–224.
43. Ranade VV, Joshi JB, Marathe AG. Flow generated by pitched bladed turbine part II: mathematical modelling and comparison with experimental data. *Chem Eng Commun*. 1989;81:225–248.
44. Jaworski Z, Dyster KN, Nienow AW. The Effect of size, location and pumping direction of pitched blade turbine impellers on flow patterns: LDA measurements and CFD predictions. *Chem Eng Res Des*. 2001;79:887–894.
45. Xureb C, Bertrand J. 3-D Hydrodynamics in a stirred tank by a double-propeller system and filled with a liquid having evolving rheological properties. *Chem Eng Sci*. 1996;51:1725–1734.
46. Kumaresan T, Joshi JB. Effect of impeller design on the flow pattern and mixing in stirred tanks. *Chem Eng J*. 2006;115:173–193.
47. Ranade VV, Mishra VP, Saraph VS, Deshpande GB, Joshi JB. Comparison of axial flow impellers using LDA. *Ind Eng Chem Res*. 1992;31:2370–2379.
48. Bittorf KJ, Kresta SM. Active volume of mean circulation for stirred tanks agitated with axial impellers. *Chem Eng Sci*. 2000;55:1325–1335.
49. Bhole MR, Joshi JB, Ramkrishna D. Population balance modeling for bubble column operating in the homogeneous regime. *AIChE J*. 2007;53:750–756.
50. Tenneti S, Garg R, Hrenya CM, Fox RO, Subramanian S. Direct numerical simulation of gas-solid suspensions at moderate Reynolds: qualifying the coupling between hydrodynamic forces and particle velocity fluctuations. *Powder Technol*. 2010;203:57–69.
51. Rewatkar VB, Joshi JB. Critical impeller speed for solid suspension in mechanically agitated three phase reactors I: experimental part. *Ind Eng Chem Res*. 1991;30:1770–1784.
52. Kulkarni AA, Joshi JB, Ravikumar V, Kulkarni BD. Application of multi-resolution analysis for simultaneous measurement of gas and liquid velocities and fractional gas hold-up in bubble column using LDA. *Chem Eng Sci*. 2001;56:5037–5048.
53. Deshpande SS, Joshi JB, Kumar VR, Kulkarni BD. Identification and characterization of flow structures in chemical process equipment using multiresolution techniques. *Chem Eng Sci*. 2008;63:5330–5346.
54. Tabib MV, Joshi JB. Analysis of dominant flow structures and their flow dynamics in industrially relevant equipment using proper orthogonal decomposition. *Chem Eng Sci*. 2008;63:3695–3715.

Manuscript received Feb. 5, 2014, and revision received May 26, 2014.